



# Constructing a novel ternary composite $(C_{16}H_{33}(CH_3)_3N)_4W_{10}O_{32}/g-C_3N_4/rGO$ with enhanced visible-light-driven photocatalytic activity for degradation of dyes and phenol

Xiaolong Yang<sup>a</sup>, Fangfang Qian<sup>a</sup>, Yan Wang<sup>b</sup>, Mengli Li<sup>c</sup>, Jinren Lu<sup>a</sup>, Yiming Li<sup>a</sup>, Mutai Bao<sup>a,\*</sup>

<sup>a</sup> Key Laboratory of Marine Chemistry Theory and Technology, Ministry of Education, Ocean University of China, 238 Song-Ling Road, Qingdao 266100, PR China

<sup>b</sup> Lanzhou Institute of Chemical Physics, Chinese Academy of Sciences, 18 Tian-Shui Road, Lanzhou 730000, PR China

<sup>c</sup> State Key Laboratory of High Performance Ceramics and Superfine Microstructure, Shanghai Institute of Ceramics, Chinese Academy of Sciences, 1295 Ding-Xi Road, Shanghai 200050, PR China



## ARTICLE INFO

### Article history:

Received 4 June 2016

Received in revised form 14 July 2016

Accepted 16 July 2016

Available online 18 July 2016

### Keywords:

$g-C_3N_4$

Decatungstate

Graphene

Visible-light-driven photocatalysis

Charge separation and transfer

## ABSTRACT

The photocatalytic performance of the  $g-C_3N_4$  photocatalyst was restricted by the low efficiency because of the fast charge recombination. The present work constructed a “killing two birds with one stone” composite  $(C_{16}H_{33}(CH_3)_3N)_4W_{10}O_{32}/g-C_3N_4$  heterostructured photocatalysts with the aim to greatly promote the charge separation and recycle decatungstate in aqueous solution. Decatungstate was immobilized on  $g-C_3N_4$  in the form of modified decatungstate  $(C_{16}H_{33}(CH_3)_3N)_4W_{10}O_{32}$  via surface bonding method for the first time. Furthermore, a novel ternary  $(C_{16}H_{33}(CH_3)_3N)_4W_{10}O_{32}/g-C_3N_4/rGO$  photocatalyst was successfully constructed by integrating graphene into the binary  $(C_{16}H_{33}(CH_3)_3N)_4W_{10}O_{32}/g-C_3N_4$  composite as the electron mediator. The photocatalysts were characterized by XRD, FTIR, FESEM, TEM, UV-vis DRS, PL and EIS measurement. The photocatalytic properties were evaluated in photodecomposition of aqueous methyl orange and phenol under visible-light irradiations. It has been shown that the obtained  $(C_{16}H_{33}(CH_3)_3N)_4W_{10}O_{32}/g-C_3N_4$  photocatalyst exhibited improved photocatalytic activity and enhanced reduced charge recombination as compared with those of  $g-C_3N_4$  and  $(C_{16}H_{33}(CH_3)_3N)_4W_{10}O_{32}$ . It has been found that the introduction of graphene revealed a synergistic effect between the  $(C_{16}H_{33}(CH_3)_3N)_4W_{10}O_{32}$  species,  $g-C_3N_4$  and graphene existed in the ternary photocatalyst. Consequently, the photocatalytic activity of the ternary  $(C_{16}H_{33}(CH_3)_3N)_4W_{10}O_{32}/g-C_3N_4/rGO$  photocatalyst was superior to that of the binary one, originating from its stronger visible-light absorption and more reduced charge combination. Finally, recycling experiments revealed that the ternary composite photocatalyst was not only highly efficient but also robust, because it can be used six times without loss of activity, which efficiently solved the problem of recycling decatungstate in reaction system. This work demonstrated that rational design and construction of  $g-C_3N_4$ -decatungstate composites could open up a new avenue for the development of new efficient visible-light photocatalysts for water disinfection.

© 2016 Elsevier B.V. All rights reserved.

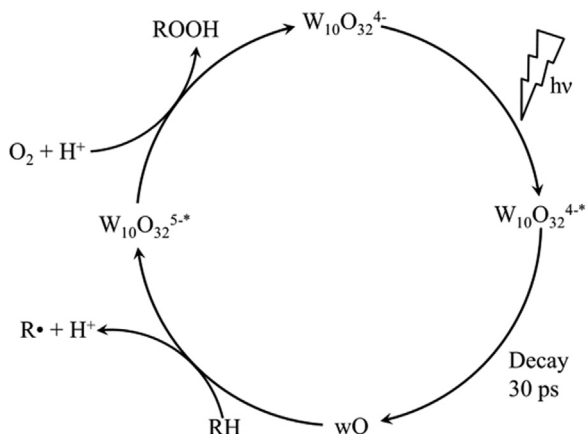
## 1. Introduction

Searching for applicable semiconductors for splitting water to produce hydrogen and photocatalytic degradation of organic pollutants has now attracted worldwide attention because of

increasingly severe energy shortage and environment pollution [1,2]. Among numerous semiconductors,  $TiO_2$  is one of the most widely used photocatalysts for water or air purification due to its low cost, low toxicity and relatively high stability. However, the photocatalytic performance is still far from satisfaction in the process of pollutant treatment due to its relatively wide band gap (3.2 eV), poor visible-light response, rapid recombination of photogenerated charges and low photocatalytic efficiency [1,3,4].

\* Corresponding author.

E-mail address: [mtbao@ouc.edu.cn](mailto:mtbao@ouc.edu.cn) (M. Bao).



**Scheme 1.** Photocatalytic behavior of decatungstate upon aerobic conditions.

Another class of photocatalytically active materials that has received somewhat less attention is the polyoxometalates (POMs), which has similar light absorption and electrochemical band-edge positions to those of  $\text{TiO}_2$ . Their unique combination of physical and chemical properties, in terms of molecular and electronic versatility, reactivity, and stability, make them a promising class of photocatalysts [5,6]. The polyoxometalate decatungstate  $\text{W}_{10}\text{O}_{32}^{4-}$ , in particular, displays interesting photocatalytic activities that are of great interest in the field of wastewater treatment [7–9]. In the presence of oxygen, irradiation of decatungstate anion with solar light ( $\lambda > 300 \text{ nm}$ ) produces the excited state that further enable organic compounds to be oxidized and particularly carbon-halogen bond to crack [7,10,11].

The proposed mechanism for decatungstate-based photocatalysis involves absorption of light by the polyanion ground state, leading to an oxygen to metal charge-transfer excited state ( $\text{W}_{10}\text{O}_{32}^{4-,*}$ ) that decays in a few picoseconds to a very reactive transient species (wO) [8,12] (Scheme 1). This species has an oxyradical-like character with a longer lifetime (about 50 nanoseconds) and is able to oxidize many substrates to their corresponding radicals with the simultaneous formation of the mono-reduced form of the decatungstate ( $\text{W}_{10}\text{O}_{32}^{5-}$ ) [8,9]. Oxidation of  $\text{W}_{10}\text{O}_{32}^{5-}$  by  $\text{O}_2$  restores the starting  $\text{W}_{10}\text{O}_{32}^{4-}$  and causes dioxygen reductive activation to peroxy species. Moreover, highly reactive hydroxyl radicals are formed through the direct reaction between photoexcited polyoxoanions and water in aqueous solutions [6,12–14].

However, in addition to its possible ability in degrading pollutants under solar irradiation, the drawback of high solubility in aqueous solution makes decatungstate hard to be recovered and recycled, impeding their potential applications. Besides, high energy gap between the well-defined HOMO-LUMO leads to low visible-light photocatalytic activity. Therefore, the design and preparation of efficient water-insoluble decatungstate photocatalysis materials with high activity and stability under visible-light, is an appealing challenge.

Many researchers have made efforts in order to resolve these problems. Incorporation of homogeneous decatungstate with support materials, such as  $\text{TiO}_2$ ,  $\text{ZrO}_2$ ,  $\text{SiO}_2$ , and some organic polymers have been extensively investigated [15,16]. Although those hybrids overcome some difficulties in recovering and recycling, other shortcomings such as limited activity or stability during the reaction are still unresolved [5]. On the other hand, semiconductor heterojunction construction has attracted a lot of attention due to its perfect effectiveness in improving the photocatalytic activity [17,18]. Recently, graphite-like carbon nitride ( $\text{g-C}_3\text{N}_4$ ), a novel metal-free direct bandgap semiconductor with a bandgap of *ca.*

2.7 eV, has attracted intense interest for its promising applications in photocatalysis, electrocatalysis, bioimaging and biomedical applications, etc [19,20]. Many kinds of composites photocatalysts have been reported to develop effective  $\text{g-C}_3\text{N}_4$ -based nanocomposites working for enhanced performance because of its inherent high recombination rate [21,22]. Although various  $\text{g-C}_3\text{N}_4$  based composites have already been obtained, few studies have focused on decatungstate- $\text{g-C}_3\text{N}_4$  heterostructured composites, which not only can resolve the problem of recycling of decatungstate but also improve the photogenerated electron-hole pair's separation of  $\text{g-C}_3\text{N}_4$  for efficiency degradation of organic pollutants.

In the current work, water-insoluble ( $\text{C}_{16}\text{H}_{33}(\text{CH}_3)_3\text{N}_4\text{W}_{10}\text{O}_{32}$  (HW) sample was designed and synthesized via surface bonding method for the first time. Followed this a novel binary HW/ $\text{g-C}_3\text{N}_4$  heterostructured photocatalysts was synthesized, it was shown that the obtained HW/ $\text{g-C}_3\text{N}_4$  photocatalyst exhibited reduced charge recombination and improved photocatalytic activity as compared with  $\text{g-C}_3\text{N}_4$  and HW. Furthermore, aiming at further increasing the photocatalytic activity of the binary photocatalyst, a novel ternary HW/ $\text{g-C}_3\text{N}_4$ /rGO (reduced Graphene Oxide) composite photocatalyst were constructed by integrating rGO into the binary one. Graphene appears to be the most promising material for effective transfer of photoelectrons due to its high electron mobility at room temperature, large specific surface area, excellent thermal conductivity, and high Young's modulus [23]. It was revealed that synergistic effect among the HW,  $\text{g-C}_3\text{N}_4$  and rGO components contributed to its stronger visible-light absorption, less charge recombination, and higher photocatalytic activity as compared with those of the binary photocatalysts. This work sheds light on a new kind of ternary photocatalysts with high visible-light driven activity for organic substrate degradation, which consists of decatungstate,  $\text{g-C}_3\text{N}_4$  and rGO. To our knowledge, this type of photocatalyst has not been reported yet.

## 2. Experimental

### 2.1. Chemicals and materials

Expandable graphite (60 mesh) was supplied by Qingdao Tianhe Graphite Co., Ltd. Melamine (99.0%), sulfuric acid (98%,  $\text{H}_2\text{SO}_4$ ), potassium permanganate ( $\text{KMnO}_4$ ), L-ascorbic acid (AR), absolute ethanol, hydrogen peroxide ( $\text{H}_2\text{O}_2$ , 30% aq.), cetyltrimethyl ammonium bromide (99%, CTAB) and hydrochloric acid (HCl) were purchased from Sinopharm Chemical Reagent Co., Ltd.  $\text{TiO}_2$  (P25, 20% rutile and 80% anatase) was obtained from Degussa (Germany). Deionized water was used during the experimental process, prepared using an ultra-pure purification system. All the chemicals were of analytically pure grade and used without further purification.

### 2.2. Preparation of bulk $\text{g-C}_3\text{N}_4$

Bulk  $\text{g-C}_3\text{N}_4$  sample was synthesized by directly heating melamine in a semi-closed system according to a previously reported procedure [24]. In a typical synthesis, 10 g of melamine was put into an alumina crucible which was heated in a muffle furnace from room temperature to 600 °C with a heating rate of 2.3 °C/min. After calcination at 600 °C for 4 h, the alumina crucible was cooled naturally to room temperature. The as-prepared  $\text{g-C}_3\text{N}_4$  was collected and ground into powder for further use.

### 2.3. Preparation of graphene oxide

Graphene oxide was prepared by a pressurized oxidation process according to a previously reported procedure [25] (Fig. S1).

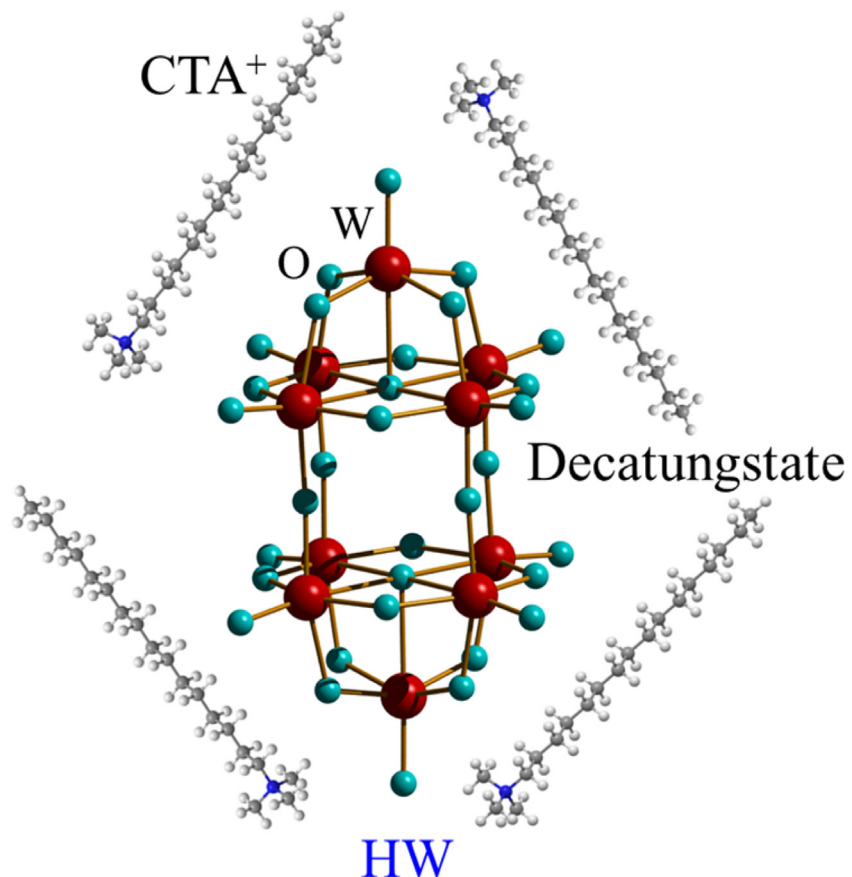


**Fig. 1.** Structures and synthesis scheme of decatungstate hybrids.

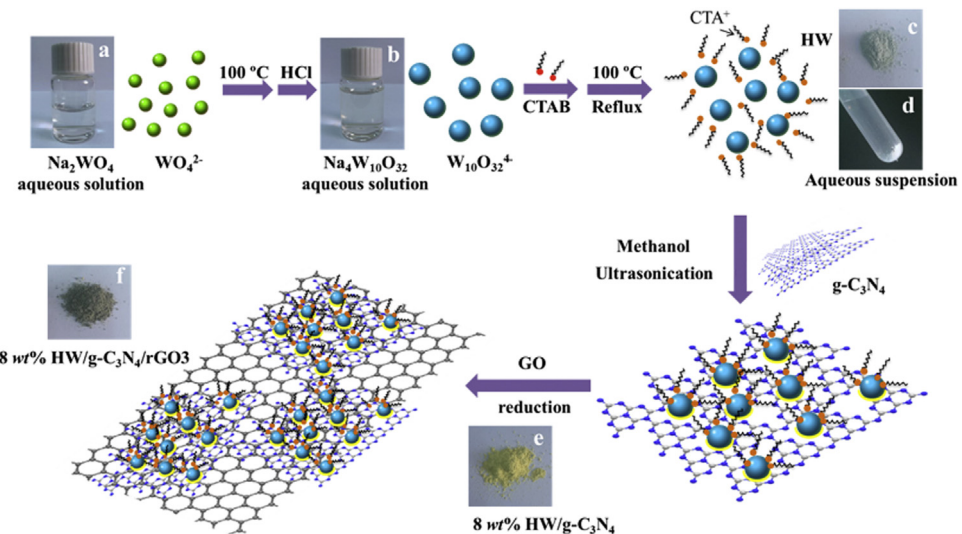


**Fig. 2.** (a–f) Schematic illustration of preparation process for  $\text{HW/g-C}_3\text{N}_4$  and  $\text{HW/g-C}_3\text{N}_4/\text{rGO}$  photocatalysts. Photograph of (a)  $\text{Na}_2\text{WO}_4$  solution, (b)  $\text{Na}_4\text{W}_{10}\text{O}_{32}$  solution, (c)  $\text{HW}$ , (d)  $\text{HW}$  aqueous suspension, (e)  $8 \text{ wt\% HW/g-C}_3\text{N}_4$ , (f)  $8 \text{ wt\% HW/g-C}_3\text{N}_4/\text{rGO3}$ .

#### 2.4. Preparation of $(\text{C}_{16}\text{H}_{33}(\text{CH}_3)_3\text{N})_4\text{W}_{10}\text{O}_{32}$ (HW)

According to a literature procedure [26], HW was prepared by mixing hot solutions of  $\text{Na}_2\text{WO}_4 \cdot 2\text{H}_2\text{O}$  (3.3 g) in water (4 mL) and 3 M  $\text{HCl}$  (6.9 mL). As shown in Fig. 1 and Fig. 2a, to the clear solution obtained after boiling for 5 min, an  $\text{H}_2\text{O}/\text{ethanol}$  solution of  $\text{CTAB}$  (1.46 g/4 mL) was added, the solution was refluxing at  $100^\circ\text{C}$  for

10 min in a 250 mL round-bottom flask (Eq. (1)). The obtained light bean green precipitate was collected by filter, washed with boiling water and ethanol, and dried at  $50^\circ\text{C}$  in vacuum for 8 h.

Dissolution test was conducted by continuous stirring of a certain amount of HW in aqueous solution. Obviously, HW is insoluble as shown in Fig. 2d. Accordingly, there was no adsorption peak

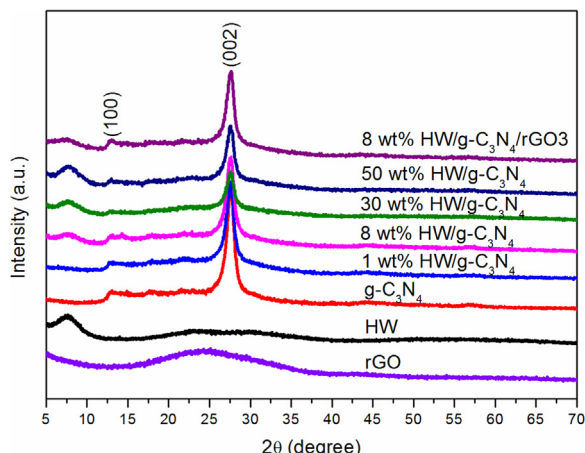
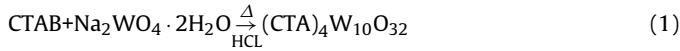


**Fig. 3.** XRD patterns of g-C<sub>3</sub>N<sub>4</sub>, HW, rGO, HW/g-C<sub>3</sub>N<sub>4</sub> and 8 wt% HW/g-C<sub>3</sub>N<sub>4</sub>/rGO3 photocatalysts.

for supernatant of HW aqueous suspension (Fig. S3), which further demonstrated that HW was indeed insoluble in water.



## 2.5. Construction of HW/g-C<sub>3</sub>N<sub>4</sub> and HW/g-C<sub>3</sub>N<sub>4</sub>/rGO composites

The typical construction of HW/g-C<sub>3</sub>N<sub>4</sub> photocatalysts (Fig. 2e) was as follows: an appropriate amount of HW and g-C<sub>3</sub>N<sub>4</sub> powder was completely dispersed in methanol assisted by ultrasonication for 0.5 h. The as prepared HW and g-C<sub>3</sub>N<sub>4</sub> suspended solution were mixed together and stirred vigorously in a fume hood for 6 h. After volatilization of the methanol, an opaque powder was obtained after drying at 60 °C overnight. In this way, a series of  $x$  wt% HW/g-C<sub>3</sub>N<sub>4</sub> photocatalysts ( $x=0, 1.0, 5.0, 8.0, 10.0, 20.0, 30.0, 40.0, 50.0, 100.0$ ) were synthesized.

To fabricate the HW/g-C<sub>3</sub>N<sub>4</sub>/rGO photocatalysts (Fig. 2f), HW and g-C<sub>3</sub>N<sub>4</sub> powder were completely dispersed in methanol assisted by ultrasonication for 0.5 h firstly. A measured amount of graphite oxide was dispersed in 150 mL of DI water and ultrasonicated for 30 min to fully exfoliate graphite oxide into graphene oxide (GO). HW and g-C<sub>3</sub>N<sub>4</sub> suspension was then added into the GO suspension and ultrasound-treated for additional 30 min. After that, the mixture was vigorously stirred for 1 h to achieve homogeneous suspension. To reduce GO in the synthesis mixture, a pre-determined amount of L-ascorbic acid (L-AA) was subsequently added [27]. The resulting mixture was stirred at 95 °C for 1.5 h, after which the reaction mixture was cooled to room temperature and washed several times with ethanol and DI water to remove excess L-AA. Finally, the as-obtained precipitate was dried at 60 °C in an

oven for 12 h. For optimization, HW/g-C<sub>3</sub>N<sub>4</sub>/rGO hybrid nanocomposites with various ratios of rGO were also constructed, which was marked as HW/g-C<sub>3</sub>N<sub>4</sub>/rGO<sub>x</sub> for the corresponding rGO content  $x$  ( $x=1.0, 3.0, 5.0\%$ ). In the meanwhile, a mechanically mixed HW-g-C<sub>3</sub>N<sub>4</sub>-rGO which contains HW, g-C<sub>3</sub>N<sub>4</sub> and rGO with the same ratio as 8 wt% HW/g-C<sub>3</sub>N<sub>4</sub>/rGO3 was also prepared by finely grinding HW, g-C<sub>3</sub>N<sub>4</sub> and rGO.

## 2.6. Photoreaction apparatus and procedure

The photocatalytic activities of obtained samples were evaluated by degrading methyl orange (MO) and phenol in aqueous solution under visible-light illumination ( $\lambda > 420$  nm). The photocatalytic degradation process was carried out in 100 mL of Pyrex double-jacket reactor. A 300 W Xe lamp (Perfect Light, PLS-SXE300) equipped with a 420 nm cut-off filter provided visible-light irradiation. The distance between the light source and the surface of the reaction solution was 10 cm. The light intensity was determined to be 150 mW/cm<sup>2</sup>. A water bath connected with a pump was used to maintain the reaction temperature at  $25 \pm 2$  °C, and a magnetic stirrer was used to keep the photocatalyst dispersed homogeneously in reaction solutions. In a typical run, 1 g/L of photocatalyst was dispersed into 50 mL MO or phenol aqueous solution with a concentration of 0.01 g/L. Prior to irradiation, the suspension was magnetically stirred in the dark for 30 min to ensure the establishment of an adsorption-desorption equilibrium. Then, at selected time intervals, 4 mL of target pollutant solution was collected and centrifuged at 12,000 rpm for 15 min to remove the photocatalyst particles from the solution. After that, the resulting supernatant was analyzed using an Ultraviolet Visible-light spectrophotometer and the characteristic absorption peak of MO at 476 nm was used to determine the extent of its decomposition. The HPLC-UV/Vis systems were carried out to analyze phenol and its degradation products can be detected using an ultraviolet absorbance detector (K 2501) operated at 275 nm coupled to a Venusil XBP-C18 (Agilent Technologies Inc.) column. Before the analysis, the samples were filtered through millipore discs of 0.45 μm to protect the chromatographic column. The mobile phase used for eluting phenol and its degradation intermediates from the HPLC columns consisted of methanol and water (60:40, v/v) at a flow rate of 1 mL/min. A blank test was also carried out on an aqueous MO solution and phenol without photocatalyst under the same condition. In addition, the recyclability of the catalyst was also studied by washing and drying the catalyst before the next cycle.

## 2.7. Structural characterization methods

The crystalline structure of the g-C<sub>3</sub>N<sub>4</sub>, HW, HW/g-C<sub>3</sub>N<sub>4</sub> and various HW/g-C<sub>3</sub>N<sub>4</sub>/rGO photocatalysts were analyzed by X-ray powder diffraction (XRD) (X'pert, PANalytical, Dutch) using Cu

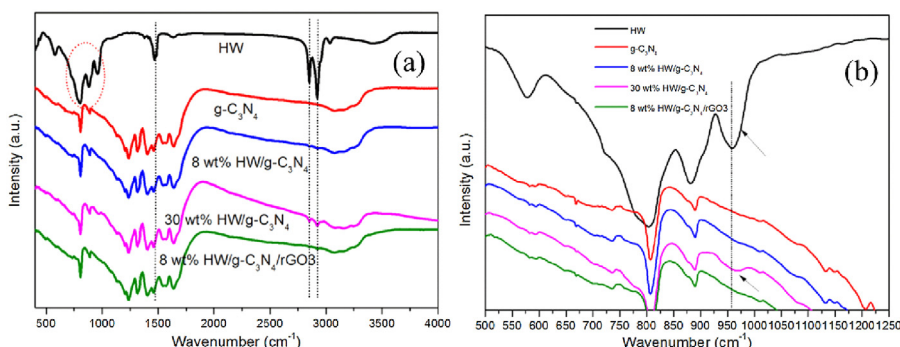


**Fig. 4.** FTIR spectra of (a) g-C<sub>3</sub>N<sub>4</sub>, HW, HW/g-C<sub>3</sub>N<sub>4</sub> and HW/g-C<sub>3</sub>N<sub>4</sub>/RGO samples. (b) Enlarged FTIR spectra from (a).

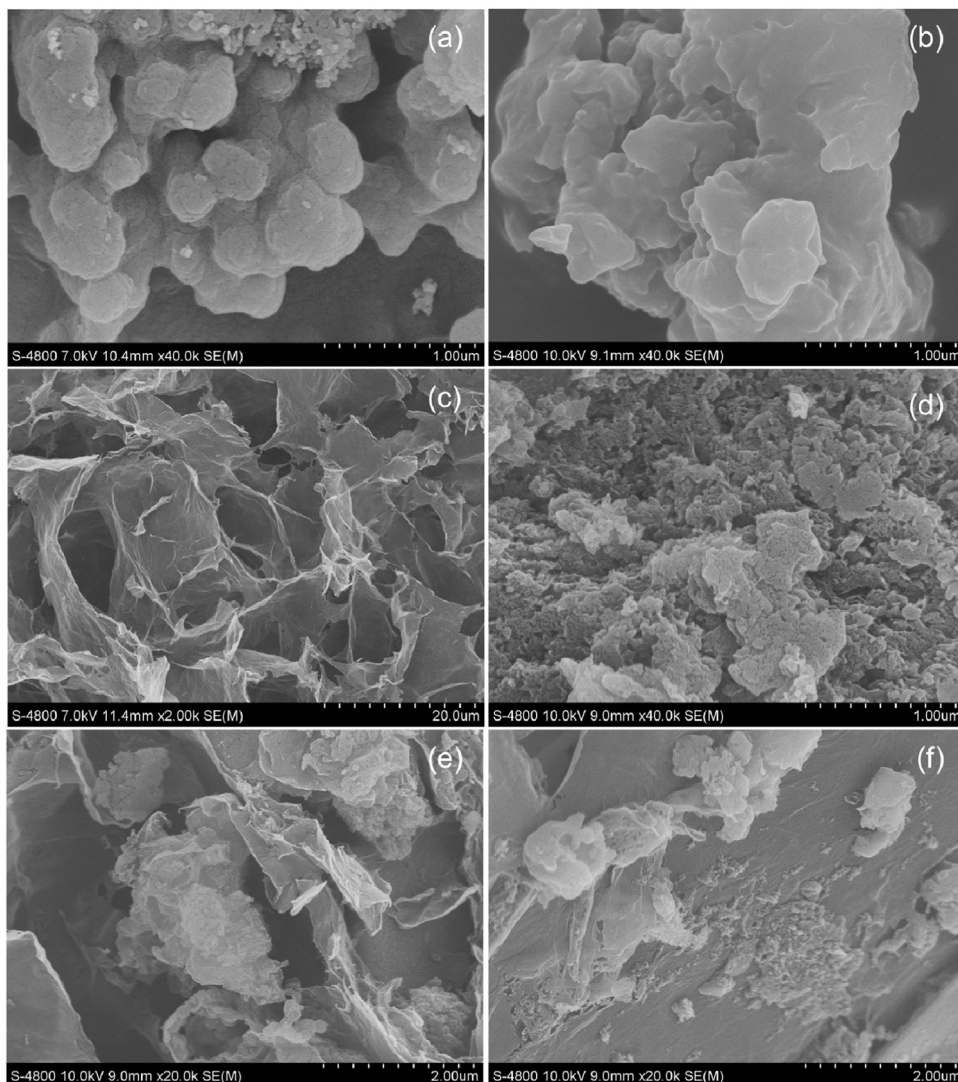


**Fig. 5.** FESEM images of (a)  $\text{g-C}_3\text{N}_4$ ; (b) HW; (c) rGO; (d) 8 wt% HW/ $\text{g-C}_3\text{N}_4$ ; (e, f) 8 wt% HW/ $\text{g-C}_3\text{N}_4$ /rGO3.

$\text{K}\alpha$  radiation ( $\lambda = 1.54050 \text{ \AA}$ ). The molecular structural information was determined from a fourier transform infrared spectroscopy (FTIR) (NEXUS 870) by the KBr pellet method in the range of 400–4000  $\text{cm}^{-1}$ . The surface morphology of the as-developed samples were examined by field emission scanning electron microscopy (FESEM) (JEOL JSM-6701F) and transmission electron microscope (TEM) (JEM-2010) with an accelerating voltage of 200 kV. Room-temperature UV-vis diffuse reflectance spectra (UV-vis DRS) were recorded on a Shimadzu UV-2550 UV-vis spectrophotometer and  $\text{BaSO}_4$  as the reference material. Absorption spectra were calculated from the reflectance data with the Kubelka-Munk function. X-ray photoelectron spectra (XPS) was taken on a photoelectron spectrometer (VG ESCALAB 210) with a monochromatic X-ray source of  $\text{Mg K}\alpha$  ( $h\nu = 1253.6 \text{ eV}$ ), calibrated internally by carbon deposit C(1s) binding energy (BE) at 284.8 eV. The photoluminescence (PL) measurements were recorded on a fluorescence spectrometer (Perkin Elmer, LS55) at room temperature. The samples were excited at a wavelength of 325 nm with a scanning speed of 600 nm/min. The width of excitation slit and emission slit was fixed at 10 nm. Electrochemical measurements were performed in a three electrode quartz cells with 0.1 M  $\text{Na}_2\text{SO}_4$  electrolyte solution. Platinum wire and saturated calomel electrode (SCE) were used as counter electrode and reference electrode, respectively, the working electrode was prepared by the doctor-blading methods as

follows. 0.1 g catalyst and two drop of Triton X-100 was grinded into fine slurries in 1 mL deionized water and coated onto FTO glass sheet, then dried at 120 °C for 12 h. The photoelectrochemical experiment results were recorded with an electrochemical system (Autolab PGSTAT302 N electrochemical workstation). The visible-light irradiation was obtained from a 300 W Xe lamp (Perfect Light, PLS-SXE300). Electrochemical impedance spectra (EIS) was measured at 0.0 V. A sinusoidal AC perturbation of 5 mV was applied to the electrode over the frequency range of 0.02–10<sup>5</sup> Hz.

### 3. Results and discussion

#### 3.1. Characterization of the HW/ $\text{g-C}_3\text{N}_4$ (/rGO) photocatalysts

The XRD patterns of pristine  $\text{g-C}_3\text{N}_4$ , HW, rGO, HW/ $\text{g-C}_3\text{N}_4$  and HW/ $\text{g-C}_3\text{N}_4$ /rGO photocatalysts are presented in Fig. 3. The two distinct peaks located at 12.8° and 27.6° of the pure  $\text{g-C}_3\text{N}_4$  sample could be indexed as (002) and (100) diffraction planes (JCPDS 87-1526), corresponding to the characteristic interplanar stacking peaks of aromatic systems and the interlayer structural packing, respectively [28]. As shown in Fig. 3, the success of the anion exchange reaction with decatungstate can be evidenced by the 7.6° diffraction peak, which is typical characteristic of decatungstate anion [29]. The XRD pattern displays a rather low crystallinity as

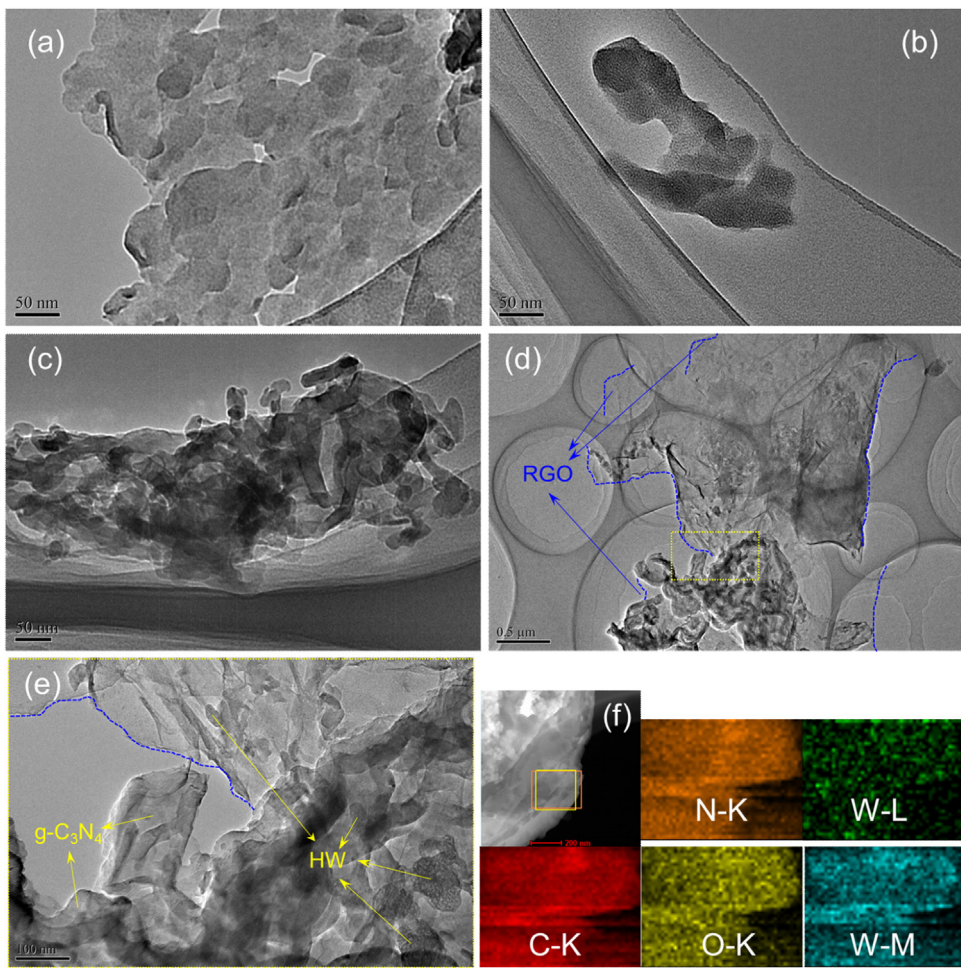


**Fig. 6.** TEM images of (a) g-C<sub>3</sub>N<sub>4</sub>; (b) HW; (c) 8 wt% HW/g-C<sub>3</sub>N<sub>4</sub>; (d), (e) 8 wt% HW/g-C<sub>3</sub>N<sub>4</sub>/rGO3; (f) Elemental mapping of 8 wt% HW/g-C<sub>3</sub>N<sub>4</sub>/rGO3.

previously reported for polyoxometallate anions intercalated into classically prepared layered double hydroxides [29]. The XRD patterns of HW/g-C<sub>3</sub>N<sub>4</sub> revealed coexistence peaks of HW and g-C<sub>3</sub>N<sub>4</sub> in the composites. There was no significant difference in diffraction pattern for 8 wt% HW/g-C<sub>3</sub>N<sub>4</sub> and 8 wt% HW/g-C<sub>3</sub>N<sub>4</sub>/rGO3, suggesting that the crystal structure and crystallization of g-C<sub>3</sub>N<sub>4</sub> and HW were not affected by the combination with graphene. The absence of the diffraction peaks for graphene might be attributed to the low content of graphene in the composite photocatalysts [30].

The functional groups of pristine g-C<sub>3</sub>N<sub>4</sub>, HW, HW/g-C<sub>3</sub>N<sub>4</sub> and HW/g-C<sub>3</sub>N<sub>4</sub>/rGO composite photocatalysts were characterized by FTIR and the results are shown in Fig. 4. For g-C<sub>3</sub>N<sub>4</sub>, the broad peak ranging from 3000 to 3500 cm<sup>-1</sup> are attributed to the N—H band and O—H stretches due to the free amino groups and adsorbed hydroxyl species, respectively. The strong bands at the 1200–1650 cm<sup>-1</sup> region are found in the spectrum, the absorption band at 1640 cm<sup>-1</sup> is attributed to C—N stretching, while the three ones at 1555 cm<sup>-1</sup>, 1461 cm<sup>-1</sup> and 1405 cm<sup>-1</sup> are contributed to the typical stretching vibration modes of C—N heterocycles. The bands at 1319 cm<sup>-1</sup> and 1243 cm<sup>-1</sup> correspond to stretching vibration of connected units of C—NH—C. In addition, the intense band located at 810 cm<sup>-1</sup> represent the characteristic breathing mode of tri-s-triazine rings units [31–33].

For HW powder sample, the absorption peaks at 2922, 2854 and 1470 cm<sup>-1</sup> are assigned to asymmetric stretching, symmetric stretching and scissor modes of —CH<sub>2</sub>— in the methylene chains, respectively [34,35]. The absorption peaks at 959 and 883, 804 cm<sup>-1</sup> can be assigned to the stretching vibrations of W=O<sub>t</sub> and

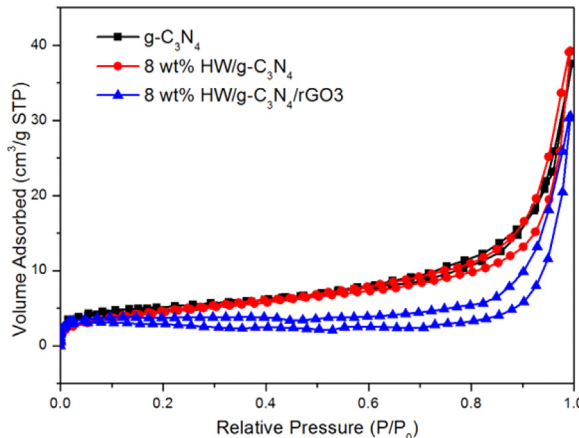
W—O<sub>b</sub>—W, respectively [16]. This indicated that the W<sub>10</sub>O<sub>32</sub><sup>4-</sup> and C<sub>16</sub>H<sub>33</sub>(CH<sub>3</sub>)<sub>3</sub>N<sup>+</sup> were integrated by anion exchange reaction.

After combination of g-C<sub>3</sub>N<sub>4</sub> and HW, the FTIR spectra showed bands related to the g-C<sub>3</sub>N<sub>4</sub> and HW materials, confirming the successful formation of the HW/g-C<sub>3</sub>N<sub>4</sub> composite. The characteristic peaks at 2922 and 2854 cm<sup>-1</sup> assigned to —CH<sub>2</sub>— in the methylene chains is present for the HW/g-C<sub>3</sub>N<sub>4</sub> composites as shown in Fig. 4(a), Fig. S4, however, characteristic peaks of W<sub>10</sub>O<sub>32</sub><sup>4-</sup> appeared till the HW content increased to 30 wt% (Fig. 4(a) and (b)). While, for the 8 wt% HW/g-C<sub>3</sub>N<sub>4</sub>/rGO3 composites, no distinct changes were observed in comparison with 8 wt% HW/g-C<sub>3</sub>N<sub>4</sub>, manifesting that the introduction of graphene species do not change the chemical structure of 8 wt% HW/g-C<sub>3</sub>N<sub>4</sub> because of the low content of graphene in the material [30,36,37].

The morphology and microstructure of the g-C<sub>3</sub>N<sub>4</sub>, HW, HW/g-C<sub>3</sub>N<sub>4</sub> and HW/g-C<sub>3</sub>N<sub>4</sub>/rGO samples were investigated by FESEM and TEM. As depicted in Figs. 5 a, 6 a , bulk g-C<sub>3</sub>N<sub>4</sub> were composed of a large number of aggregated morphology with a large size and lamellar structure, which is the typical structure characteristic of g-C<sub>3</sub>N<sub>4</sub> synthesized by the polymerization method [38,39]. The representative morphology of HW appeared as irregular agglomerates with varying sizes (Figs. 5 b, 6 b). It is noteworthy that graphene flakes were uniformly covered on HW and g-C<sub>3</sub>N<sub>4</sub> component (Fig. 6d), and well interconnect with the g-C<sub>3</sub>N<sub>4</sub> and HW, resulting in the intimate interfacial contact between g-C<sub>3</sub>N<sub>4</sub>, HW and graphene. Elemental mapping images further verified the uniform distribution of W element throughout HW/g-C<sub>3</sub>N<sub>4</sub>/rGO

**Table 1**The BE of C 1s, N 1s, W 4f<sub>7/2</sub> and O 1s for various samples (eV).

Element Sample	C 1s <sup>a</sup>	N 1s		W 4f <sub>7/2</sub>	O 1s
g-C <sub>3</sub> N <sub>4</sub>	288.3	398.7	399.8	401.3	404.4
HW	281.2	398.2		402.5	
8 wt% HW/g-C <sub>3</sub> N <sub>4</sub>	281.2	395.3	396.6	398.0	400.9
8 wt% HW/g-C <sub>3</sub> N <sub>4</sub> /rGO3	281.1	395.3	396.5	397.9	400.9

<sup>a</sup> The BE of standard reference carbon (284.8 eV) was not shown.**Fig. 7.** N<sub>2</sub> adsorption-desorption isotherms.

at nanoscale as shown in Fig. 6f. It was beneficial for the strong interaction among three components.

The N<sub>2</sub> adsorption-desorption isotherms of the g-C<sub>3</sub>N<sub>4</sub>, HW/g-C<sub>3</sub>N<sub>4</sub> and HW/g-C<sub>3</sub>N<sub>4</sub>/rGO samples are shown in Fig. 7 (Fig. 9b-f, Table 1). The adsorption-desorption isotherms of all the samples were characteristic of Type IV Brunauer-Deming-Deming-Teller classification, which is usually associated with capillary condensation in mesopores (2–50 nm) [40]. This result was in agreement with the SEM and TEM results. Additionally, these isotherms display H3 hysteresis loops, which may be pertinent to the mesopores that are induced by sample stacking [41]. Mesopores can allow light to reflect and penetrate deep into the pores of the photocatalyst and lead to high mobility of charges, which result in enhanced photocatalytic activity [42,43]. The Brunauer-Emmett-Teller (BET) specific surface area of g-C<sub>3</sub>N<sub>4</sub>, 8 wt% HW/g-C<sub>3</sub>N<sub>4</sub> and 8 wt% HW/g-C<sub>3</sub>N<sub>4</sub>/rGO3 was 17.1, 16.6 and 23.8 m<sup>2</sup>/g, respectively. The surface areas of HW/g-C<sub>3</sub>N<sub>4</sub> do not change much compared with that of the ternary composites because the quantity of graphene in the composites was rather low.

The optical adsorption properties of HW, g-C<sub>3</sub>N<sub>4</sub>, HW/g-C<sub>3</sub>N<sub>4</sub> and HW/g-C<sub>3</sub>N<sub>4</sub>/rGO samples were characterized by UV-vis diffuse reflectance spectroscopy and the corresponding spectra are shown in Fig. 8. It was observed that pure g-C<sub>3</sub>N<sub>4</sub> shows absorption wavelengths from the UV to the visible range, which can be assigned to the intrinsic band gap of g-C<sub>3</sub>N<sub>4</sub>, corresponding to the reported optical band gap at around 2.7 eV [44,45]. Notably, decatungstate present an intense absorption at wavelengths lower than 400 nm [12], whereas the absorption edges of the HW significantly extend to the region of visible-light wavelength (<450 nm). The HW/g-C<sub>3</sub>N<sub>4</sub> samples exhibited the similar characteristic absorption edge as pure g-C<sub>3</sub>N<sub>4</sub>, indicating the basic framework of the host g-C<sub>3</sub>N<sub>4</sub> almost stayed unchanged after the hybridization. The absorption edges of HW become more evident with the increase of HW content in the heterostructured samples. Furthermore, compared with the absorption spectrum of HW/g-C<sub>3</sub>N<sub>4</sub>, the HW/g-C<sub>3</sub>N<sub>4</sub>/rGO sample displayed a wide absorption ranging from 250 to 800 nm, indicating the introduction of graphene has a positive effect on the optical property [46,47]. On account of the improved optical adsorption

property, it was anticipated that the HW/g-C<sub>3</sub>N<sub>4</sub>/rGO photocatalyst can achieve more efficient utilization of visible-light and therefore show enhanced visible-light-driven photocatalytic activity.

The band gap energies of semiconductors can be estimated by Kubelka-Munk transformation,  $\alpha h\nu = A(h\nu - E_g)^{n/2}$ , where  $\alpha$  represents the absorption coefficient,  $\nu$  is the light frequency,  $E_g$  is the band gap energy,  $A$  is a constant and  $n$  depends on the characteristics of the transition in a semiconductor [48,49]. For g-C<sub>3</sub>N<sub>4</sub>, the value of  $n$  is 4 for the indirect transition [48]. Thus, the band gap energy ( $E_g$ ) estimated from the intercept of the tangents to the plots of  $(\alpha h\nu)^{1/2}$  vs photon energy were 2.70 and 2.72 eV for g-C<sub>3</sub>N<sub>4</sub> and 8 wt% HW/g-C<sub>3</sub>N<sub>4</sub>, respectively, as shown in Fig. 8b. This could be ascribed to the enhancement of the UV range adsorption of HW due to hybridization.

The XPS measurements were carried out to investigate the chemical environment and surface stoichiometry of the elements of samples. The survey XPS spectrum of g-C<sub>3</sub>N<sub>4</sub> (Fig. 9a) revealed that the elements of C, O, and N existed on the surface of pristine g-C<sub>3</sub>N<sub>4</sub>, while the elements of C, O, N and W can be detected in HW, which indicated that Br<sup>-</sup> is replaced completely by W<sub>10</sub>O<sub>32</sub><sup>4-</sup> with an ion-exchange method. The W element was also found for the 8 wt% HW/g-C<sub>3</sub>N<sub>4</sub> and 8 wt% HW/g-C<sub>3</sub>N<sub>4</sub>/rGO3 composites besides C, O and N elements. The corresponding high resolution spectra of C 1s, N 1s, W 4f and O 1s are also given. The XPS spectra of the C 1s core level for g-C<sub>3</sub>N<sub>4</sub> can be deconvoluted into two components including the standard reference carbon (284.8 eV) and the sp<sup>2</sup>-bonded C in N=C(-N)<sub>2</sub> (288.3 eV) (Fig. 9b). With regard to the N 1s spectrum, there exhibits three N states including pyridinic-N (398.7 eV), triazine rings C=N-C (401.3 eV) and tertiary nitrogen N-(C)<sub>3</sub> (399.8 eV) [50] (Fig. 9c), which are the three N units that constituted the basic units of g-C<sub>3</sub>N<sub>4</sub>. Another peak centered at 404.4 eV is associated to charging effect or positive charge localization in heterocycles. These assignments of C 1s and N 1s agree well with the g-C<sub>3</sub>N<sub>4</sub> reported previously [36,51,52].

The XPS spectrum of the C 1s core level for HW can be deconvoluted into two components including the standard reference carbon (284.8 eV) and the -CH<sub>2</sub>- in the methylene chains (286.2 eV) (Fig. 9b). Compared with pure CTAB (Fig. S5), the C 1s feature peaks originated from -CH<sub>2</sub>- in the methylene chains of HW shift toward the higher binding energy side, indicative of a strong chemical interaction between C<sub>16</sub>H<sub>33</sub>(CH<sub>3</sub>)<sub>3</sub>N<sup>+</sup> and W<sub>10</sub>O<sub>32</sub><sup>4-</sup> anion with the surface bonding method. The N 1s spectrum of HW displayed two peaks centering at 402.5 and 398.2 eV. The peak at 402.5 eV can be ascribed to C<sub>16</sub>H<sub>33</sub>(CH<sub>3</sub>)<sub>3</sub>N<sup>+</sup> [53], and the peak at 398.2 eV possibly can be assigned to W-N bond, because there was only peak located at 402.0 eV ascribed to C<sub>16</sub>H<sub>33</sub>(CH<sub>3</sub>)<sub>3</sub>N<sup>+</sup> for pure CTAB (Fig. S6). The high resolution W 4f XPS spectrum displayed two main peaks at 35.5 and 37.7 eV, which can be identified to W 4f<sub>7/2</sub> and W 4f<sub>5/2</sub>, respectively [54]. The O 1s spectrum (Fig. 9f) of HW can be deconvoluted into two peaks, and the binding energies of 530.5 and 532.0 eV can be ascribed to oxygen in tungstate-oxo cluster and hydroxyl groups, respectively. Obviously, the C 1s feature peaks originated from the sp<sup>2</sup>-bonded C in N=C(-N)<sub>2</sub> (288.3 eV) of g-C<sub>3</sub>N<sub>4</sub> shift toward the lower binding energy side (281.2 eV) when forming the 8 wt% HW/g-C<sub>3</sub>N<sub>4</sub> heterostructure, (Fig. 9b, Table 1), indicative of a strong chemical interaction between HW and g-C<sub>3</sub>N<sub>4</sub> in the

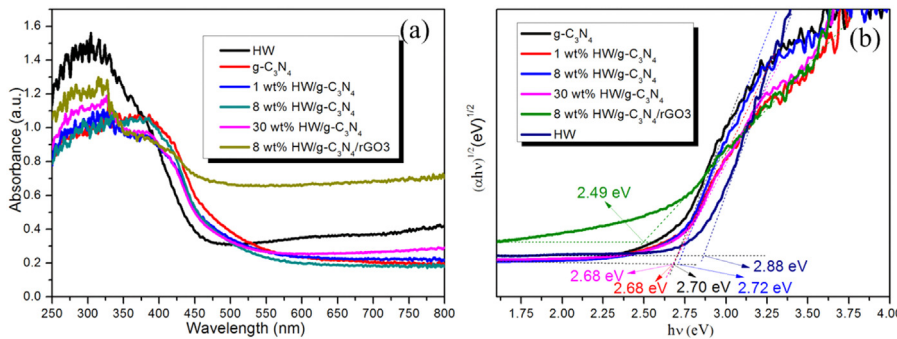


**Fig. 8.** (a) UV-vis diffuse reflectance spectra of the photocatalysts and (b) their corresponding band gap plots.

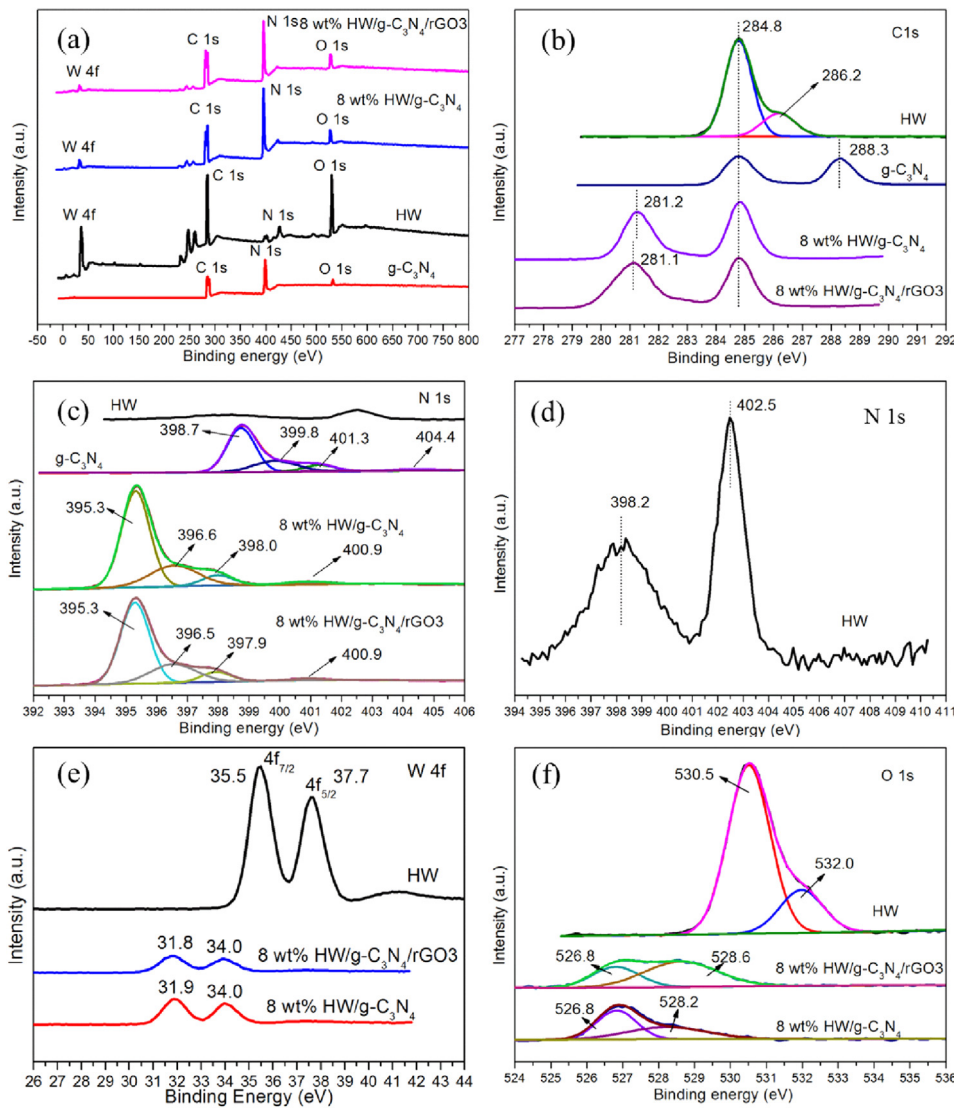


**Fig. 9.** XPS spectra of  $\text{g-C}_3\text{N}_4$ , HW, 8.0 wt% HW/ $\text{g-C}_3\text{N}_4$  and 8.0 wt% HW/ $\text{g-C}_3\text{N}_4$ /rGO3. (a) survey; (b) C 1s; (c, d) N 1s; (e) W 4f; (f) O 1s.

binary composites. Similar changes were also observed for the BE of N 1s, W 4f and O 1s. Specifically, W 4f<sub>7/2</sub> feature peaks of HW shifted toward the lower binding energy side (31.8 eV), which was close to the BE of W 4f<sub>7/2</sub> of WC (31.5–32.0), indicative of a strong reduction reaction for  $\text{W}_{10}\text{O}_{32}^{4-}$  which occurred over the surface of HW and  $\text{g-C}_3\text{N}_4$  for HW/ $\text{g-C}_3\text{N}_4$  composites. Notably, bulk phase

of HW immobilized on the  $\text{g-C}_3\text{N}_4$  was still be  $\text{W}_{10}\text{O}_{32}^{4-}$  (Fig. 4(b)), such band forming phenomenon was mainly occurred over the surface of HW. Corresponding C 1s feature peak also supported such hypothesis, it was found that  $sp^2$ -bonded C in  $\text{N}=\text{C}(\text{—N})_2$  of  $\text{g-C}_3\text{N}_4$  (288.3 eV) shifted toward the lower binding energy side (281.2 eV), which was close to the BE of C 1s of WC (282.5 eV) although it seems

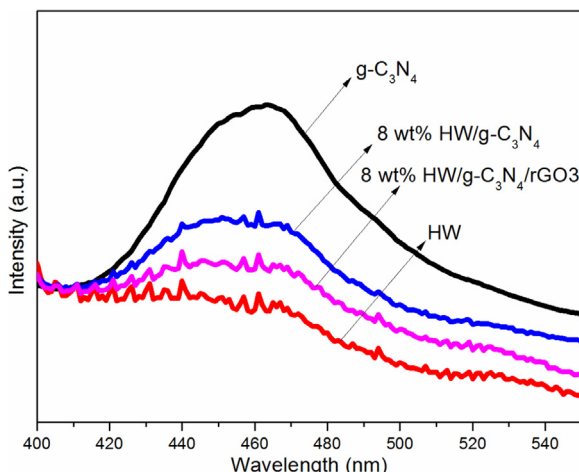


**Fig. 10.** Photoluminescence emission spectra of  $\text{g-C}_3\text{N}_4$ , HW, 8 wt% HW/ $\text{g-C}_3\text{N}_4$ , and 8 wt% HW/ $\text{g-C}_3\text{N}_4/\text{rGO3}$ . The wavelength of excitation light for photoluminescence emission spectra is 325 nm.

like such reaction proceeds incompletely. As a polymer sheet constituted with tri-*s*-triazine, each layer of  $\text{g-C}_3\text{N}_4$  is considered as a multistage polymerized weak base. Both bridge nitrogen atom, which connects the tri-*s*-triazine units, and the heterocyclic nitrogen atom are tertiary ammonium groups that could participate in salt formations [55]. Furthermore,  $\text{g-C}_3\text{N}_4$  contains so-called “nitrogen pots”, which are filled with six nitrogen lone-pair electrons and are potentially ideal sites for metal inclusion [56]. The “pots” built by the tri-*s*-triazine units will provide structural space for W of  $\text{W}_{10}\text{O}_{32}^{4-}$  anion.

Photoluminescence (PL) analysis was performed to study the interfacial charge transfer and the separation efficiency of photogenerated electrons and holes. Higher PL intensity indicates a higher recombination of charge carriers [57]. PL spectra of  $\text{g-C}_3\text{N}_4$ , HW and their composites 8 wt% HW/ $\text{g-C}_3\text{N}_4$ , and 8 wt% HW/ $\text{g-C}_3\text{N}_4/\text{rGO3}$  are shown in Fig. 10. The main emission peak was centered at about 460 nm for pure  $\text{g-C}_3\text{N}_4$ , which could be attributed to the band-band PL phenomenon due to the down-transfer of the photoinduced charge carriers of  $\text{g-C}_3\text{N}_4$  [58]. Compared with  $\text{g-C}_3\text{N}_4$ , the addition of HW or rGO hardly changed the emission peak position, but rather reduced its relative intensity, indicating the combination with HW species played a key role in reducing the recombination between electrons and holes. The charge recombination was further reduced for the ternary composites, the excellent electrical conductivity property of graphene could facilitate the delivering of the photo-induced carriers to the active sites, resulting in reduction in charge recombination for the composite photocatalysts containing graphene [59,60].

The separation efficiency of photo-generated electrons and holes plays an important role in enhancing photocatalytic activity. The interface charge separation efficiency can be investigated using EIS method. Fig. 11 shows the EIS Nyquist plots of samples under visible-light illumination. A smaller arc radius of the EIS Nyquist plot reflects a higher efficient charge transfer occurring at the interface [55,58]. Therefore, the 8 wt% HW/ $\text{g-C}_3\text{N}_4$  as well as 8 wt% HW/ $\text{g-C}_3\text{N}_4/\text{rGO3}$  exhibited more effective separation of photo-generated charge carriers due to its smaller arc radius. These results indicated that the introduction of HW can dramatically enhance the separation and transfer efficiency of photo-generated electron-hole pairs. Accordingly, both the electron collecting and transporting properties of graphene in the nanocomposites contributed to the obvious reduction of electron-hole recombination and would remarkably enhance the photocatalytic properties of the as-obtained nanocomposites.

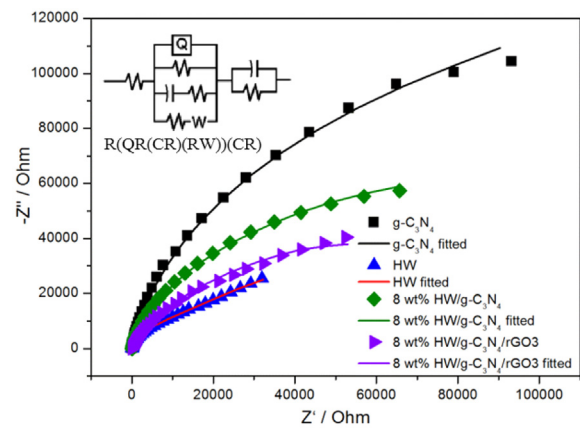


**Fig. 11.** EIS Nyquist plots of the  $\text{g-C}_3\text{N}_4$ , HW, 8 wt% HW/ $\text{g-C}_3\text{N}_4$  and 8 wt% HW/ $\text{g-C}_3\text{N}_4/\text{rGO3}$  photocatalysts under the irradiation of visible light. (0.1 M  $\text{Na}_2\text{SO}_4$  aqueous solution, bias voltage was set at 5 mV versus SCE).

### 3.2. Photocatalytic properties of the HW/ $\text{g-C}_3\text{N}_4$ (/rGO) photocatalysts

The photocatalytic activity of HW/ $\text{g-C}_3\text{N}_4$  and HW/ $\text{g-C}_3\text{N}_4/\text{rGO}$  composites were evaluated by the degradation of representative industrial dye methyl orange (MO, Fig. 12) and colorless organic molecule phenol (Fig. 13). On the basis of a blank experiment, the self-photolysis of MO could be neglected (Fig. S7). For a pure HW and  $\text{g-C}_3\text{N}_4$ , the concentration of MO was only reduced by about 13.8 and 60.8% after 3 h of visible-light irradiation. Two-component composites containing 1, 5, 8, 10, 20, 30, 40 and 50 wt% HW showed higher photocatalytic activity, and the concentrations of MO were reduced by about 68.9, 75.7, 89.7, 86.8, 85.5, 84.4, 84.1 and 80.0%, respectively (Fig. 12a). It can be seen that the photocatalytic activity was enhanced with the nominal mass fraction of HW to  $\text{g-C}_3\text{N}_4$  increasing from 1 wt% to (8–10) wt%, suggesting that the HW played an important role in promoting the photocatalytic activity of binary composites. However, as the nominal mass fraction further increased to 40%, a decrease in photocatalytic activity happened. It can be inferred that increase in mass fraction of the HW species in the binary photocatalyst would cause more defects and induce a shielding effect on  $\text{g-C}_3\text{N}_4$  [30], thus decreasing its photocatalytic activity. Compared with the single-component samples and two-component samples, the ternary composite of heterostructured HW/ $\text{g-C}_3\text{N}_4/\text{rGO}$ (1, 3, 5 wt%) photocatalysts exhibited remarkably enhanced photocatalytic activity, the concentration of MO was reduced by about 88.6, 99.0 and 97.0%, respectively (Fig. 12b). It should be noted that 8 wt% HW/ $\text{g-C}_3\text{N}_4/\text{rGO3}$  sample showed the highest photocatalytic activity owing to its strong visible-light absorption (Fig. 8a). As a contrast experiment, the photocatalytic performance of the HW- $\text{g-C}_3\text{N}_4$ -rGO was measured, and the degradation rate was only 73%, which was inferior to those for the HW/ $\text{g-C}_3\text{N}_4$ (/rGO) composites. Note that the photocatalytic decomposition of MO was supposed to follow a pseudo-first-order kinetics reaction [61]. As shown in Fig. S8, Fig. 12c, the kinetic constant of 8 wt% HW/ $\text{g-C}_3\text{N}_4/\text{rGO3}$  was estimated to be  $0.02234 \text{ min}^{-1}$ , which was 1.8, 1.9 and 4.1 times bigger than those of 8 wt% HW/ $\text{g-C}_3\text{N}_4$  ( $0.01235 \text{ min}^{-1}$ ),  $\text{g-C}_3\text{N}_4/\text{rGO3}$  ( $0.01188 \text{ min}^{-1}$ ) and  $\text{g-C}_3\text{N}_4$  ( $0.005410 \text{ min}^{-1}$ ), respectively. As interlayers, graphene harassed the HW as well as  $\text{g-C}_3\text{N}_4$  inside the samples and participated in electrical conduction and bridged the gap between  $\text{g-C}_3\text{N}_4$  and HW, facilitating the separation of photoexcited charge and reducing the recombination possibility of the photogenerated electrons and holes. During the photocatalysis characterization of the photocatalyst samples, the concentration of total organic carbon (TOC) was evaluated and the results are illus-

trated in Fig. 12d. Obviously, the rate of decolorization was much faster than that of mineralization. The TOC value of MO was reduced by about 16.4% and 35.0% after 3 h of visible-light irradiation for g-C<sub>3</sub>N<sub>4</sub> and 8 wt% HW/g-C<sub>3</sub>N<sub>4</sub>/rGO3 photocatalysts, which showed the evidence of the decomposition of MO into carbon dioxide but at a relatively slow rate.

Because the phenol compound is known to be a highly toxic, persistent and biorecalcitrant pollutant, and its presence in ground

and surface water is considered to be a direct threat to the health of humankind [62]. Due to the poor oxidation ability of g-C<sub>3</sub>N<sub>4</sub> associated with the relative high level of VB position, it is difficult for the g-C<sub>3</sub>N<sub>4</sub> itself to degrade phenol. Generally, the pure g-C<sub>3</sub>N<sub>4</sub> was hardly to make decomposition of phenol, only giving 27.0% removal efficiency in 6 h (Fig. 13a). In contrast, the binary HW/g-C<sub>3</sub>N<sub>4</sub> and ternary HW/g-C<sub>3</sub>N<sub>4</sub>/rGO composites demonstrated a higher activity than pure g-C<sub>3</sub>N<sub>4</sub>. Phenol could be removed at about 52.8%

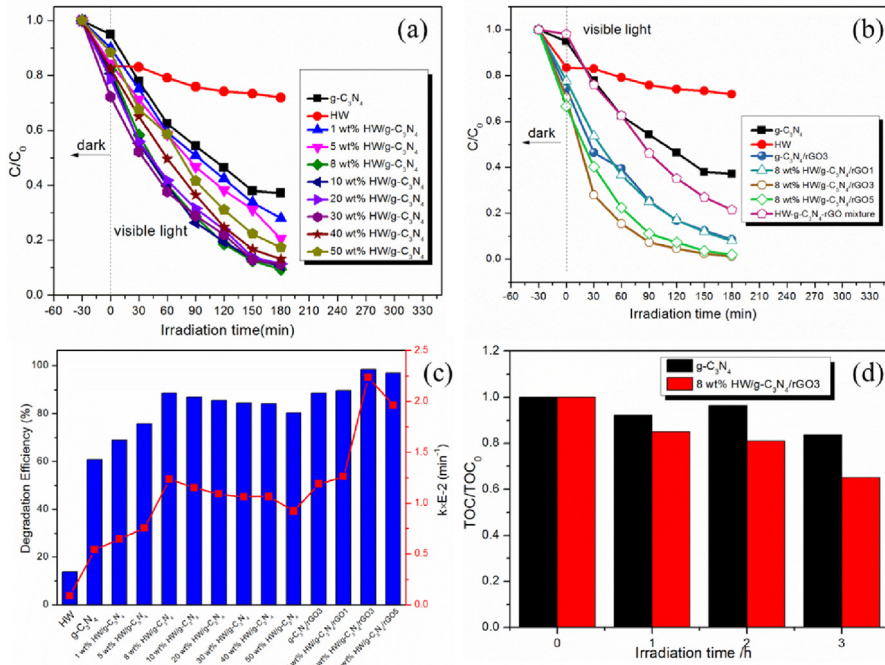


**Fig. 12.** (a, b) Photocatalytic activity (c) decolorization efficiency of the prepared samples on degradation of MO under visible light irradiation ( $\lambda > 420$  nm). (d) TOC removal of MO over g-C<sub>3</sub>N<sub>4</sub> and 8 wt% HW/g-C<sub>3</sub>N<sub>4</sub>/rGO3 composites.

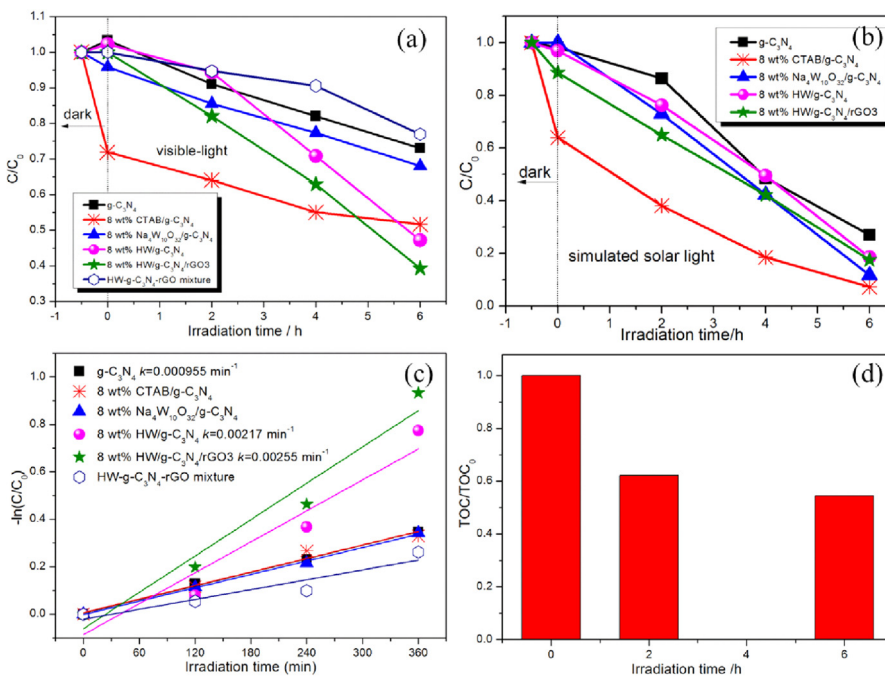


**Fig. 13.** (a) Comparison of the degradation efficiency of phenol in the presence of pure g-C<sub>3</sub>N<sub>4</sub>, CTAB/g-C<sub>3</sub>N<sub>4</sub>, Na<sub>4</sub>W<sub>10</sub>O<sub>32</sub>/g-C<sub>3</sub>N<sub>4</sub>, HW/g-C<sub>3</sub>N<sub>4</sub> and HW/g-C<sub>3</sub>N<sub>4</sub>/rGO composites under visible-light and (b) simulated solar light irradiation (320–780 nm) (Fig. S9). (c) Apparent rate constant  $k$  under visible-light irradiation. (d) TOC removal of phenol over 8 wt% HW/g-C<sub>3</sub>N<sub>4</sub>/rGO3 composites under visible-light illumination.

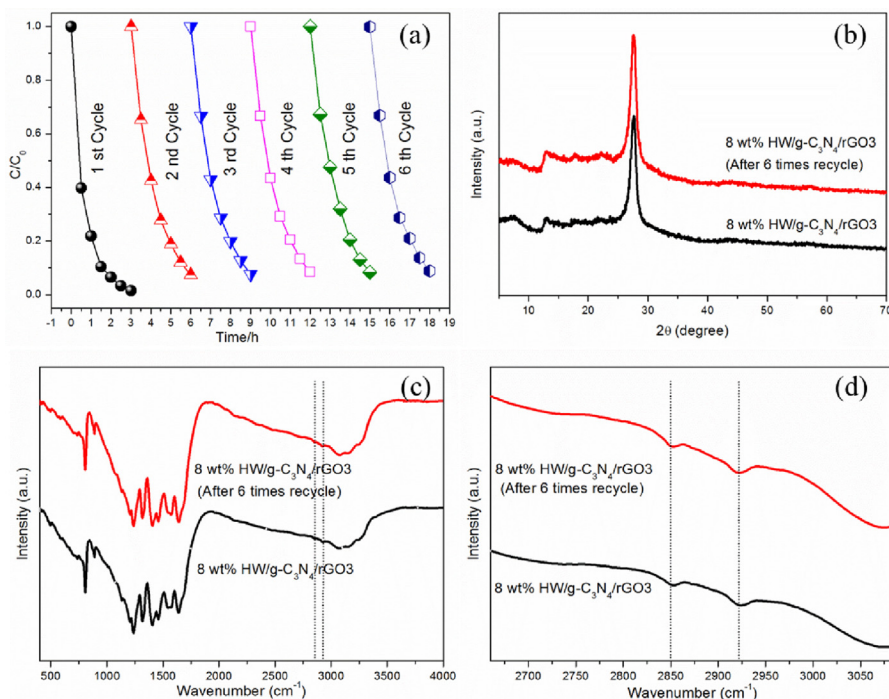


**Fig. 14.** (a) Cycle runs of 8 wt% HW/g-C<sub>3</sub>N<sub>4</sub>/rGO composites for degradation of MO under visible-light irradiation ( $\lambda > 420$  nm). (b) XRD patterns before and after the cycle runs. (c) FTIR spectra before and after the cycle runs. (d) Enlarged FTIR spectra from (c).

and 60.7% using 8 wt% HW/g-C<sub>3</sub>N<sub>4</sub> and 8 wt% HW/g-C<sub>3</sub>N<sub>4</sub>/rGO3 as photocatalysts (Fig. 13a). In addition, 8 wt% CTAB/g-C<sub>3</sub>N<sub>4</sub> and 8 wt% Na<sub>4</sub>W<sub>10</sub>O<sub>32</sub>/g-C<sub>3</sub>N<sub>4</sub> were also compared in order to understand the effect of HW on binary photocatalyst although we know Na<sub>4</sub>W<sub>10</sub>O<sub>32</sub> and CTAB would run off due to its high solubility in aqueous [10,63]. Obviously, 8 wt% CTAB/g-C<sub>3</sub>N<sub>4</sub> showed relatively strong adsorption capacity but poor in the coming photocatalysis reaction, while the behavior of the 8 wt% Na<sub>4</sub>W<sub>10</sub>O<sub>32</sub>/g-C<sub>3</sub>N<sub>4</sub> was similar with that of the pure g-C<sub>3</sub>N<sub>4</sub> under visible-light irradiation, which manifested that photocatalytic activity cannot be improved by the simple physical mixed method, the maximum absorption wavelength of Na<sub>4</sub>W<sub>10</sub>O<sub>32</sub> aqueous solution is concentrated in the ultraviolet region of 323 nm [12]. The kinetic constant of 8 wt% HW/g-C<sub>3</sub>N<sub>4</sub>/rGO3 was estimated to be 0.00255 min<sup>-1</sup>, which was 2.7 times bigger than that of g-C<sub>3</sub>N<sub>4</sub> (0.000955 min<sup>-1</sup>).

It was necessary to investigate the corresponding photocatalytic activity of HW/g-C<sub>3</sub>N<sub>4</sub>(rGO) photocatalysts under full spectrum light irradiation. As shown in Fig. 13b, 8 wt% HW/g-C<sub>3</sub>N<sub>4</sub> and 8 wt% HW/g-C<sub>3</sub>N<sub>4</sub>/rGO3 composites demonstrated a higher activity than pure g-C<sub>3</sub>N<sub>4</sub> (81.5, 82.5% and 73.0%, respectively). Apparently, W<sub>10</sub>O<sub>32</sub><sup>4-</sup> anion played an important role in degradation reaction under full spectrum light irradiation as we expected. It was more evident that 8 wt% Na<sub>4</sub>W<sub>10</sub>O<sub>32</sub>/g-C<sub>3</sub>N<sub>4</sub> showed even higher degradation efficiency (88.3%) compared with 8 wt% HW/g-C<sub>3</sub>N<sub>4</sub> and 8 wt% HW/g-C<sub>3</sub>N<sub>4</sub>/rGO3 composites, which was assigned to the high solubility of Na<sub>4</sub>W<sub>10</sub>O<sub>32</sub> in aqueous, other than heterogeneous photocatalysis reaction, the degradation efficiency was enhanced because the reaction molecule and W<sub>10</sub>O<sub>32</sub><sup>4-</sup> anion were conducted freely in homogeneous photocatalysis reaction.

Furthermore, the TOC value of phenol was reduced by about 55.5% after 6 h of visible-light irradiation for 8 wt% HW/g-C<sub>3</sub>N<sub>4</sub>/rGO3 photocatalysts. The experimental results clearly demonstrated that the combination of HW with g-C<sub>3</sub>N<sub>4</sub> led to superior degradation performance under visible-light irradiation. More significantly, compared with 8 wt% HW/g-C<sub>3</sub>N<sub>4</sub>, 8 wt% HW/g-C<sub>3</sub>N<sub>4</sub>/rGO3 exhibited much higher photocatalytic activity, owing to its stronger visible-light absorption (Fig. 8a) and the much

smaller charge recombination possibility in the ternary composite (Figs. 10 and 11).

For evaluating the recyclability of the 8 wt% HW/g-C<sub>3</sub>N<sub>4</sub>/rGO3 composite, the additional experiments were carried out to degrade MO under visible-light irradiation for six times. After the complete degradation of MO, the catalyst was collected by centrifugation, washed with deionized water several times, dried in an oven at 60 °C for 12 h and then used for the next run. As shown in Fig. 14a, degradation efficiency declined to 92.6% in the second cycle and no significant drop can be found for the following cycle runs. The hybrid photocatalyst was found to be reusable and considerable photoactivity was achieved after the sixth run. The removal efficiency was maintained at around 91.1% in the 6th recycling test. Degradation efficiency in the first run was 90.0% for phenol removal under simulated solar light irradiation, which declined to 72.6% in the second cycle and maintained at around 68.5% in the 4th recycling test (Fig. S11). No distinct change was found for the ternary photocatalyst after experiencing cycling runs as shown in XRD patterns (Fig. 14b) and FTIR spectra (Fig. 14c and d).

### 3.3. Proposed reaction mechanism of the HW/g-C<sub>3</sub>N<sub>4</sub>(rGO) photocatalysts

All of h<sup>+</sup>, e<sup>-</sup>, •O<sub>2</sub><sup>-</sup> and •OH are possible active species for the photodegradation of organic pollutants [33,64,65]. Photogenerated electrons from g-C<sub>3</sub>N<sub>4</sub> could reduce surface chemisorbed O<sub>2</sub> to superoxide radicals (•O<sub>2</sub><sup>-</sup>) (E(O<sub>2</sub><sup>-</sup>/O<sub>2</sub>) = -0.33 eV vs. NHE) [33]. Hydroxyl radicals (•OH) can be generated from •O<sub>2</sub><sup>-</sup> [65]. To evaluate the role of these active species, individual scavengers were added to the photodegradation system. The scavengers used are isopropanol (IPA) for •OH, ammonium oxalate (AO) for h<sup>+</sup> and N<sub>2</sub> purging for •O<sub>2</sub><sup>-</sup> [30,66].

Fig. 15a shows that the addition of IPA or bubbling N<sub>2</sub> caused the degradation efficiency of MO decreased to 47.1% and 22.6%. After AO was added, the photocatalytic efficiency was almost invariable (52.6%). This indicated that •OH and •O<sub>2</sub><sup>-</sup> were significant active species in the photocatalytic process of g-C<sub>3</sub>N<sub>4</sub> only, while

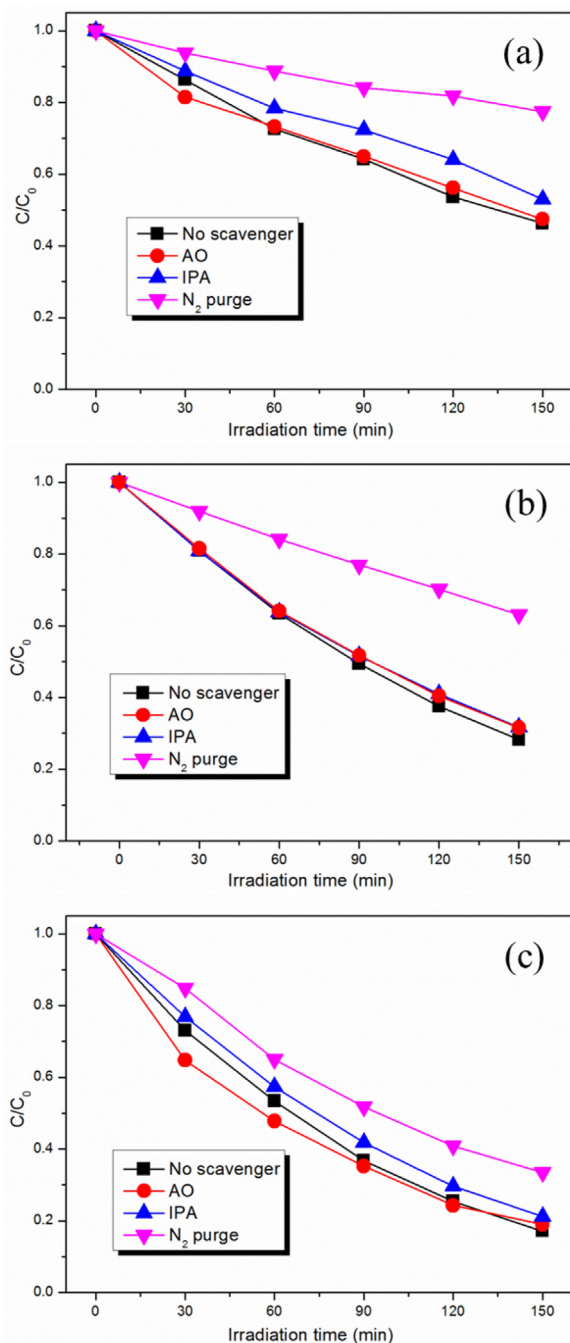


**Fig. 15.** Effect of a series of scavengers on the photocatalytic efficiencies of photocatalysts. (a)  $\text{g-C}_3\text{N}_4$ ; (b) 8.0 wt% HW/ $\text{g-C}_3\text{N}_4$  (c) 8 wt% HW/ $\text{g-C}_3\text{N}_4/\text{rGO3}$ . (The dosage of scavengers = 0.1 mmol L<sup>-1</sup>, illumination time  $t = 150$  min).

the holes were not the major reactive species. Thus, the influencing degree was as follows,  $\bullet\text{O}_2^- > \bullet\text{OH} > \text{h}^+$ , which agrees well with the previous reports [66]. Fig. 15b shows the MO degradation efficiency of the 8.0 wt% HW/ $\text{g-C}_3\text{N}_4$  photocatalyst was 71.8% without scavenger. Photodegradation activity was barely changed after the addition of IPA or AO. A significant suppression of photocatalytic performance was observed when  $\text{N}_2$  was bubbled (36.9%), confirming the important role of  $\bullet\text{O}_2^-$  in the photodegradation process. Fig. 15c shows that the addition of IPA or bubbling  $\text{N}_2$  made the degradation efficiency of MO decreased from 99.0% to 78.8% and 66.5%, respectively. While the addition of AO enhanced the photocatalytic efficiency especially in the initial period, because the photooxidation capability of  $\text{g-C}_3\text{N}_4$  is moderate, it is considered

that the slow consumption of photogenerated holes in VB is the rate-determining step in MO degradation [67]. The addition of AO alleviated the kinetic bottleneck of photodegradation process for  $\text{g-C}_3\text{N}_4$ , since the oxidation of  $\text{C}_2\text{O}_4^{2-}$  to  $\text{CO}_2$  was favorable from the point of dynamics. Obviously, photogenerated holes were not the active species,  $\bullet\text{OH}$  and  $\bullet\text{O}_2^-$  were the major reactive species for the 8 wt% HW/ $\text{g-C}_3\text{N}_4/\text{rGO3}$  photocatalyst. The influencing degree was as follows,  $\bullet\text{O}_2^- > \bullet\text{OH} > \text{h}^+$ .

Different semiconductor materials have different Fermi level potentials. The opposite movement of the Fermi levels of two semiconductors would lead to a new balance of the Fermi level when forming a new composite. With the shift of the Fermi level, electrons and holes will exchange on the interface between them and an interfacial electric field will be built [68]. The Mott-Schottky method was employed to determine the electronic potentials of  $\text{g-C}_3\text{N}_4$ , HW and their composites (Fig. 16). According to the tangent slopes in Fig. 16, both  $\text{g-C}_3\text{N}_4$  and HW photoelectrodes exhibited the characteristics of *n*-type semiconductors. The flatband potential of a semiconductor material can be determined by extrapolating to  $C^{-2} = 0$ . The flatband potentials of  $\text{g-C}_3\text{N}_4$  and HW were approximately -1.19 and -0.35 V (vs. SCE), respectively. While, that of the HW/ $\text{g-C}_3\text{N}_4$  composite positively shifted to -0.32 V. The difference in their flatband potentials demonstrated that a heterojunction electric field was formed on the interface between  $\text{g-C}_3\text{N}_4$  and HW. The existence of this electric field significantly increased the separation efficiency of the photogenerated electrons and holes and therefore dramatically enhanced the photocatalytic degradation performance of the HW/ $\text{g-C}_3\text{N}_4$  composite as discussed above. The measured potentials can be converted to the normal hydrogen electrode (NHE) scale via the Nernst equation (Eq. (2)):

$$E(\text{NHE}) = E(\text{SCE}) + 0.24 \quad (2)$$

The calculated CB edges of  $\text{g-C}_3\text{N}_4$  and HW were -0.95 eV and -0.35 eV, respectively. With the band gap energies shown in Fig. 8b, the VB edges of  $\text{g-C}_3\text{N}_4$  and HW were 1.75 eV and 2.53 eV, respectively. Thus, it could be concluded that the VB top of HW was lower than that of  $\text{g-C}_3\text{N}_4$ , while the CB bottom of  $\text{C}_3\text{N}_4$  was higher than that of HW. On the basis of the above results and previous reports [64,69], a possible mechanism for the enhanced photocatalytic activity over the present HW/ $\text{g-C}_3\text{N}_4/\text{rGO}$  is shown schematically in Fig. 17. Since the CB edge potential of  $\text{g-C}_3\text{N}_4$  (-0.95 eV) was more negative than that of HW (-0.35 eV), the photoexcited electrons on  $\text{g-C}_3\text{N}_4$  could transfer to the CB of HW driven by CB offset of 0.6 eV, whereas the photogenerated holes transferred from HW to  $\text{g-C}_3\text{N}_4$  driven by VB offset of 0.78 eV. The potential difference was the main driving force for efficient charge separation and transfer. As the photogenerated electrons and holes were spatially separated into two different components, the charge recombination was drastically inhibited, which was of great benefit for enhancing the photocatalytic activity [69]. In addition, it is known that the work function of rGO is 0.02 V lower than the CB minimum of  $\text{TiO}_2$  which located at -0.56 V vs NHE [70]. It can serve as an excellent acceptor and trap for photoexcited electrons, hence the photoinduced electrons could be quickly transferred to the graphene, and then can be trapped by  $\text{O}_2$ . In such a way, the photoexcited electron-hole pairs could be effectively separated further [3,40,71]. Hence, with the help of graphene, heterostructured photocatalysts would greatly suppress the recombination of electrons and holes, and thus result in an enhanced photocatalytic activity of  $\text{g-C}_3\text{N}_4/\text{HW}/\text{rGO}$ .

#### 4. Conclusion

Based on the above systematic investigations, the following conclusions are drawn (1) Visible-light-responsive HW/ $\text{g-C}_3\text{N}_4/\text{rGO}$  composites were successfully developed via introducing  $\text{W}_{10}\text{O}_{32}^{4-}$

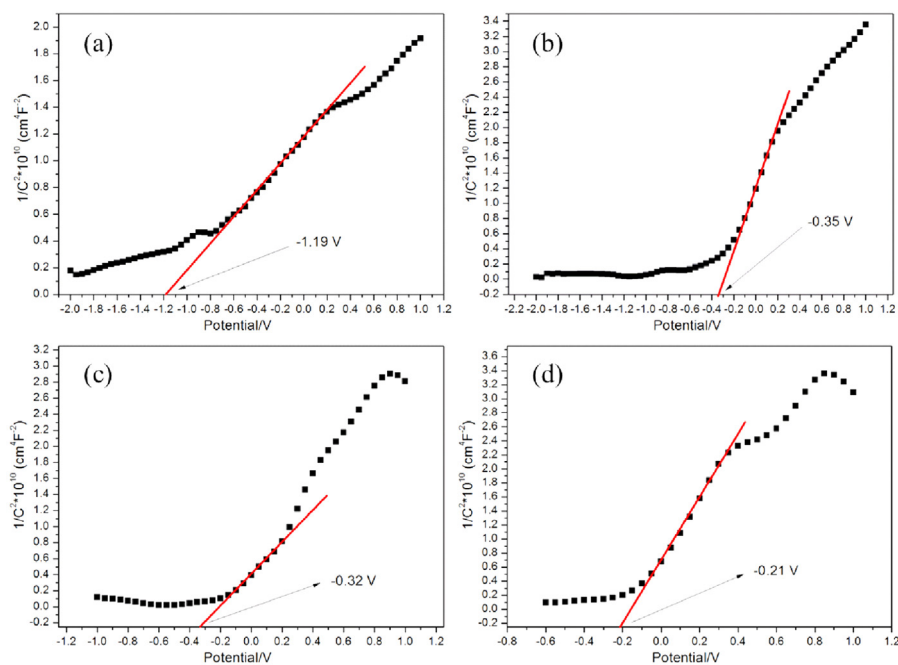


**Fig. 16.** Mott-Schottky plots collected for (a)  $\text{g-C}_3\text{N}_4$  (b) HW (c) 8 wt% HW/ $\text{g-C}_3\text{N}_4$  and (d) 8 wt% HW/ $\text{g-C}_3\text{N}_4/\text{rGO}_3$  at a frequency of 1000 Hz in the dark. (0.1 M  $\text{Na}_2\text{SO}_4$ , vs SCE).

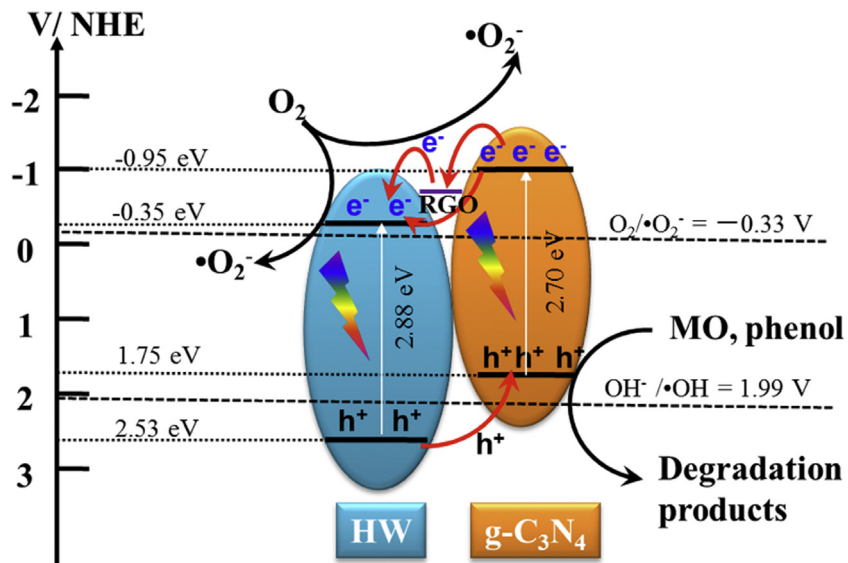


**Fig. 17.** Schematic illustration of electron-hole separation and transport in the HW/ $\text{g-C}_3\text{N}_4$  and HW/ $\text{g-C}_3\text{N}_4/\text{rGO}$  composites photocatalyst.

polyanion to  $\text{g-C}_3\text{N}_4$  photocatalyst by surface bonding method. (2) XPS revealed that an intimate interaction between the surface of modified decatungstate and  $\text{g-C}_3\text{N}_4$  formed in the heterostructured composites. (3) The 8.0 wt% ( $\text{C}_{16}\text{H}_{33}(\text{CH}_3)_3\text{N}_4$ ) $/W_{10}\text{O}_{32}/\text{g-C}_3\text{N}_4/\text{rGO}$ (3.0 wt%) exhibited the highest photocatalytic activity, which showed a reaction rate constant as high as 0.02234 and  $0.002550 \text{ min}^{-1}$ , 4.1 and 2.7 times higher than that of bare  $\text{g-C}_3\text{N}_4$  for the photodegradation of methyl orange and phenol, respectively. It possessed good stability and durability. (4) In the degradation of methyl orange,  $\bullet\text{O}_2^-$  and  $\bullet\text{OH}$  species played a major role and the role of  $\text{h}^+$  were negligible. (5) Such a remarkable enhancement of photocatalytic activity was mainly attributed to the improved separation and transfer of photogenerated electron-hole pairs at the interface of HW/ $\text{g-C}_3\text{N}_4/\text{rGO}$  composites, which could be ascribed to the well-aligned overlapping band structures

of  $\text{g-C}_3\text{N}_4$ , HW and graphene. This work not only open new perspectives for developing new efficient and stable photocatalytic systems addressed to clean wastewater containing aromatic hydrocarbons, but also provides relevant information for the future functionalized decatungstate- $\text{g-C}_3\text{N}_4$  design of heterostructured composite semiconductors applied in the field of energy and environment.

#### Conflict of interest

The authors declare no competing financial interest.

#### Acknowledgments

This research is financially supported by the National Natural Science Foundation of China (21403257, 41376084) and Postdoc-

toral Research Project of Qingdao, China (861605040004). This is MCTL Contribution No.126.

## Appendix A. Supplementary data

Supplementary data associated with this article can be found, in the online version, at <http://dx.doi.org/10.1016/j.apcatb.2016.07.024>.

## References

- [1] T. Morikawa, R. Asahi, H. Irie, T. Ohwaki, *Chem. Rev.* 114 (2014) 9824–9852.
- [2] Y. Ma, X.L. Wang, Y.S. Jia, X.B. Chen, H.X. Han, C. Li, *Chem. Rev.* 114 (2014) 9987–10043.
- [3] S.W. Zhang, J.X. Li, X.K. Wang, Y.S. Huang, M.Y. Zeng, J.Z. Xu, *J. Mater. Chem. A* 3 (2015) 10119–10126.
- [4] H.H. Chen, C.E. Nanayakkara, V.H. Grassian, *Chem. Rev.* 112 (2012) 5919–5948.
- [5] L. Zhang, B.Q. Shan, H.X. Yang, D.S. Wu, R. Zhu, J.H. Nie, R. Cao, *RSC Adv.* 5 (2015) 23556–23562.
- [6] A. Hiskia, A. Mylonas, E. Papaconstantinou, *Chem. Soc. Rev.* 30 (2001) 62–69.
- [7] M.D. Tzirakis, I.N. Lykakis, M. Orfanopoulos, *Chem. Soc. Rev.* 38 (2009) 2609–2621.
- [8] C. Tanielian, *Coord. Chem. Rev.* 178–180 (1998) 1165–1181.
- [9] A. Maldotti, A. Molinari, R. Amadelli, *Chem. Rev.* 102 (2002) 3811–3836.
- [10] A. Allaoui, M.A. Malouki, P. Wong-Wah-Chung, *Chemosphere* 85 (2011) 558–564.
- [11] S. Rafqah, P.W. Chung, C. Forano, M. Sarakha, *J. Photochem. Photobiol. A: Chem.* 199 (2008) 297–302.
- [12] A. Molinari, G. Magnacca, G. Papazzoni, A. Maldotti, *Appl. Catal. B: Environ.* 138–139 (2013) 446–452.
- [13] A. Molinari, A. Maldotti, A. Bratovic, G. Magnacca, *Catal. Today* 206 (2013) 46–52.
- [14] A. Molinari, R. Argazzi, A. Maldotti, *J. Mol. Catal. A: Chem.* 372 (2013) 23–28.
- [15] R.R. Ozer, J.L. Ferry, *Environ. Sci. Technol.* 35 (2001) 3242–3246.
- [16] S. Farhadi, S. Sepahvand, *J. Mol. Catal. A: Chem.* 318 (2010) 75–84.
- [17] X.H. Li, M. Antonietti, *Chem. Soc. Rev.* 42 (2013) 6593–6604.
- [18] H.L. Wang, L.S. Zhang, Z.G. Chen, J.Q. Hu, S.J. Li, Z.H. Wang, J.S. Liu, X.C. Wang, *Chem. Soc. Rev.* 43 (2014) 5234–5244.
- [19] X.C. Wang, S. Blechert, M. Antonietti, *ACS Catal.* 2 (2012) 1596–1606.
- [20] Y. Wang, X.C. Wang, M. Antonietti, *Angew. Chem. Int. Ed.* 51 (2012) 68–89.
- [21] Y. Hou, Z.H. Wen, S.M. Cui, X.R. Guo, J.H. Chen, *Adv. Mater.* 25 (2013) 6291–6297.
- [22] Y.B. Li, H.M. Zhang, P.R. Liu, D. Wang, Y. Li, H.J. Zhao, *Small* 9 (2013) 3336–3344.
- [23] N. Gao, X. Fang, *Chem. Rev.* 115 (2015) 8294–8343.
- [24] X.D. Zhang, X. Xie, H. Wang, J.J. Zhang, B.C. Pan, Y. Xie, *J. Am. Chem. Soc.* 135 (2013) 18–21.
- [25] C.L. Bao, L. Song, W.Y. Xing, B.H. Yuan, C.A. Wilkie, J.L. Huang, Y.Q. Guo, Y. Hu, *J. Mater. Chem.* 22 (2012) 6088–6096.
- [26] A. Maldotti, A. Molinari, G. Varani, M. Lenarda, L. Storaro, F. Bigi, R. Maggi, A. Mazzacani, G. Sartori, *J. Catal.* 209 (2002) 210–216.
- [27] J.L. Zhang, H.J. Yang, G.X. Shen, P. Cheng, J.Y. Zhang, S.W. Guo, *Chem. Commun.* 46 (2010) 1112–1114.
- [28] G.G. Zhang, S.H. Zang, X.C. Wang, *ACS Catal.* 5 (2015).
- [29] E.S. Da Silva, V. Prevot, C. Forano, P. Wong-Wah-Chung, H.D. Burrows, M. Sarakha, *Environ. Sci. Pollut. Res.* 21 (2014) 11218–11227.
- [30] Q. Liu, Y.R. Guo, Z.H. Chen, Z.G. Zhang, X.M. Fang, *Appl. Catal. B: Environ.* 183 (2016) 231–241.
- [31] Z. Zhu, Z.Y. Lu, D.D. Wang, X. Tang, Y.S. Yan, W.D. Shi, Y.S. Wang, N.L. Gao, X. Yao, H.J. Dong, *Appl. Catal. B: Environ.* 182 (2016) 115–122.
- [32] Z.Y. Zhang, J.D. Huang, M.Y. Zhang, Q. Yuan, B. Dong, *Appl. Catal. B: Environ.* 163 (2015) 298–305.
- [33] H.P. Li, J.Y. Liu, W.G. Hou, N. Du, R.J. Zhang, X.T. Tao, *Appl. Catal. B: Environ.* 160–161 (2014) 89–97.
- [34] Y.C. Qu, W.X. Wang, L.Q. Jing, S. Song, X. Shi, L.P. Xue, H.G. Fu, *Appl. Surf. Sci.* 257 (2010) 151–156.
- [35] Y.H. Li, S. Zhang, C.L. Ma, H.D. Li, J. Lumin. 126 (2007) 661–664.
- [36] K. Dai, L.H. Lu, C.H. Liang, G.P. Zhu, Q.Z. Liu, L. Geng, J.Q. He, *Dalton Trans.* 44 (2015) 7903–7910.
- [37] Y.H. Li, Y.J. Sun, F. Dong, W.K. Ho, *J. Colloid Interface Sci.* 436 (2014) 29–36.
- [38] L.Y. Chen, W.D. Zhang, *Appl. Surf. Sci.* 301 (2014) 428–435.
- [39] J.L. Lin, Z.M. Pan, X.C. Wang, *ACS Sustain. Chem. Eng.* 2 (2014) 353–358.
- [40] R.C. Pawar, V. Khare, C.S. Lee, *Dalton Trans.* 43 (2014) 12514–12527.
- [41] L. Wang, J. Ding, Y.Y. Chai, Q.Q. Liu, J. Ren, X. Liu, W.L. Dai, *Dalton Trans.* 44 (2015) 11223–11234.
- [42] C.Y. Wang, H. Zhang, F. Li, L.Y. Zhu, *Environ. Sci. Technol.* 44 (2010) 6843–6848.
- [43] C.S. Guo, M. Ge, L. Liu, G.D. Gao, Y.C. Feng, Y.Q. Wang, *Environ. Sci. Technol.* 44 (2010) 419–425.
- [44] J. Xu, L.W. Zhang, R. Shi, Y.F. Zhu, *J. Mater. Chem. A* 1 (2013) 14766–14772.
- [45] Y.J. Yao, F. Lu, Y.P. Zhu, F.Y. Wei, X.T. Liu, C. Lian, S.B. Wang, *J. Hazard. Mater.* 297 (2015) 224–233.
- [46] B. Ai, X.G. Duan, H.Q. Sun, X. Qiu, S.B. Wang, *Catal. Today* 258 (2015) 668–675.
- [47] W.Y. Gao, M.Q. Wang, C.X. Ran, L. Li, *Chem. Commun.* 51 (2015) 1709–1712.
- [48] X. Xin, J.Y. Lang, T.T. Wang, Y.G. Su, Y.X. Zhao, X.J. Wang, *Appl. Catal. B: Environ.* 181 (2016) 197–209.
- [49] W.J. Shan, Y. Hu, Z.G. Bai, M.M. Zheng, C.H. Wei, *Appl. Catal. B: Environ.* 188 (2016) 1–12.
- [50] Q. Liu, J.Y. Zhang, *Langmuir* 29 (2013) 3821–3828.
- [51] K. Dai, L.H. Lu, Q. Liu, G.P. Zhu, X.Q. Wei, J. Bai, L.L. Xuan, H. Wang, *Dalton Trans.* 43 (2014) 6295–6299.
- [52] C.Y. Xu, Q. Han, Y. Zhao, L.X. Wang, Y. Li, L.T. Qu, *J. Mater. Chem. A* 3 (2015) 1841–1846.
- [53] X.H. Liu, X.H. Luo, S.X. Lu, J.C. Zhang, W.L. Cao, *J. Colloid Interface Sci.* 307 (2007) 94–100.
- [54] P. Niu, J.C. Hao, *Colloids Surf. A* 431 (2013) 127–132.
- [55] X.R. Du, G.J. Zou, Z.H. Wang, X.L. Wang, *Nanoscale* 7 (2015) 8701–8706.
- [56] X.C. Wang, X.F. Chen, A. Thomas, X.Z. Fu, M. Antonietti, *Adv. Mater.* 21 (2009) 1609–1612.
- [57] D.L. Jiang, L.L. Chen, J.J. Zhu, M. Chen, W.D. Shi, J.M. Xie, *Dalton Trans.* 42 (2013) 15726–15734.
- [58] M.L. Li, L.X. Zhang, X.Q. Fan, Y.J. Zhou, M.Y. Wu, J.L. Shi, *J. Mater. Chem. A* 3 (2015) 5189–5196.
- [59] W.J. Ong, L.L. Tan, S.P. Chai, S.T. Yong, A.R. Mohamed, *Nano Energy* 13 (2015) 757–770.
- [60] X.M. Lv, J.Y. Shen, J.X. Wang, Z.S. Cui, J.M. Xie, *RSC Adv.* 5 (2015) 15993–15999.
- [61] Y. Zhao, J. Chu, S.H. Li, Y. Chen, G.P. Sheng, Y.P. Chen, W.W. Li, G. Liu, Y.C. Tian, Y. Xiong, H.Q. Yu, *Chem. Eng. J.* 170 (2011) 440–444.
- [62] W.J. Liao, M. Muruganathan, Y.R. Zhang, *Phys. Chem. Chem. Phys.* 17 (2015) 8877–8884.
- [63] Y.H. Guo, C.W. Hu, X.L. Wang, Y.H. Wang, E.B. Wang, *Chem. Mater.* 13 (2001) 4058–4064.
- [64] F.J. Zhang, F.Z. Xie, S.F. Zhu, J. Liu, J. Zhang, S.F. Mei, W. Zhao, *Chem. Eng. J.* 228 (2013) 435–441.
- [65] Y.J. Wang, R. Shi, J. Lin, Y.F. Zhu, *Energy Environ. Sci.* 4 (2011) 2922–2929.
- [66] S.F. Chen, Y.F. Hu, S.G. Meng, X.L. Fu, *Appl. Catal. B: Environ.* 150–151 (2014) 564–573.
- [67] S. Chu, Y. Wang, Y. Guo, J.Y. Feng, C.C. Wang, W.J. Luo, X.X. Fan, Z.G. Zou, *ACS Catal.* 3 (2013) 912–919.
- [68] Y.Y. Bu, Z.Y. Chen, C. Feng, W.B. Li, *RSC Adv.* 4 (2014) 38124–38132.
- [69] F. Dong, Z.W. Zhao, T. Xiong, Z.L. Ni, W.D. Zhang, Y.J. Sun, W.K. Ho, *ACS Appl. Mater. Interfaces* 5 (2013) 11392–11401.
- [70] W.J. Wang, Jimmy C. Yu, D.H. Xia, P.K. Wong, Y.C. Li, *Environ. Sci. Technol.* 47 (2013) 8724–8732.
- [71] Q.J. Xiang, J.G. Yu, M. Jaroniec, *J. Am. Chem. Soc.* 134 (2012) 6575–6578.